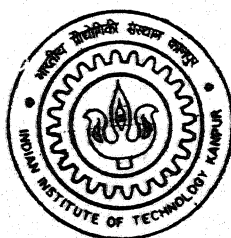


# FLOW AND HEAT TRANSFER CHARACTERISTICS IN A THREE DIMENSIONAL RIBBED CHANNEL

by  
MEENA SINGH



TH  
ME/2000/M  
Si 64 f

DEPARTMENT OF MECHANICAL ENGINEERING  
INDIAN INSTITUTE OF TECHNOLOGY KANPUR

February, 2000

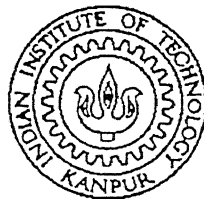
# **FLOW AND HEAT TRANSFER CHARACTERISTICS IN A THREE DIMENSIONAL RIBBED CHANNEL**

A Thesis Submitted  
in Partial Fulfillment of the Requirements  
for the Degree of

**MASTER OF TECHNOLOGY**

by

**MEENA SINGH**



**Department of Mechanical Engineering  
Indian Institute of Technology  
Kanpur - India**

February, 2000

75 MAY 2000/ME

CENTRAL LIBRARY  
I. I. T., KANPUR

~~130876~~

TH  
ME/2000/M  
8642



A130876

## CERTIFICATE

29-2-2000  
Wbpl

It is certified that the work contained in the thesis entitled **Flow and Heat transfer Characteristics in a Three Dimensional Ribbed Channel** by Meena Singh, has been carried out under our supervision and that this work has not been submitted elsewhere for a degree.

*P. K. Panigrahi*

Dr. P. K. Panigrahi  
Department of Mechanical Engineering  
IIT Kanpur

*Gautam Biswas*

Dr. Gautam Biswas  
Department of Mechanical Engineering  
IIT Kanpur

February, 2000

To  
my grandmother

## ABSTRACT

For high thermal efficiency the advanced aeroengines use high temperature gas ( 1400 - 1500° C ) at the entry of the turbines. Often such temperature is well above the allowable metal temperature. Therefore, highly efficient cooling technologies such as film cooling, impingement cooling, and rib augmented cooling are employed for the turbine blades. Various experimental and numerical investigations have addressed the issues of augmentation of heat transfer in the narrow aspect ratio channels with rib turbulators (see Han et al. (1989); Durao et al. (1991) and Acharya et al. (1994)). The presence of ribs leads to complex flow fields with regions of flow separation before and after the ribs.. Each interruption in the flow field due to the surface mounted rib enables the velocity distribution to be more homogeneous and a new boundary layer starts developing downstream of the rib. The heat transfer is primarily enhanced due to the decrease in the thermal resistance owing to the thinner boundary layers on the interrupted surfaces. Another reason for heat transfer enhancement can be attributed to the mixing induced by large scale structures present downstream of the separation point.

The present work is an attempt to study the time dependent velocity field around a pair of symmetrically placed ribs on the walls of a three dimensional rectangular channel. A modified version of Marker-And-Cell algorithm (Harlow and Welch, 1965) has been employed to solve the unsteady incompressible Navier-Stokes and energy equations. The flow structures is presented with the help of instantaneous velocity vector and vorticity fields, FFT and time averaged and rms values of components of velocity. The spanwise averaged Nusselt number is found to increase at the locations of reattachment. The numerical results have been compared with the experimental results of Panigrahi (1997).

## Acknowledgements

I take this opportunity to express my deep regards, whole hearted gratitude and thanks to my thesis supervisors Dr. G. Biswas and Dr. P. K. Panigrahi for their constant co-operation and encouragement throughout the course of the research.

I gratefully acknowledge Dr. V. Eswaran for his invaluable suggestion, help and encouragement throughout the work. I take great pleasure in acknowledging the help of my father Shri R.S.Singh, MECON, Ranchi for giving a wider perspective of mechanical engineering applications.

I have no words to acknowledge the help and cooperation of Kajoridi whose confidence in my capabilities was a source of great inspiration throughout. I am thankful to all my friends in Fluid mechanics laboratory Dr.Arun Saha, Pavitrada, Mr. R.Magesh, Ms Tanuja, Ghata, Ashish, Atul, Mr.S.Tewari for their sincere co-operation and help. I am especially thankful to Sameer for his whole-hearted cooperation throughout the work. I acknowledge special thanks to Sushanta for helping me in writing up my thesis. I am thankful to Sambhunath Sharma for his help. I acknowledge the cooperation of many of my friends who made my stay at the institute a memorable one.

Last but not the least, the silent support, good wishes and blessing of my parents and other family members has been the source of my inspiration throughout my research work.

Meena Singh

# Contents

Certificate	ii
Dedication	iii
Abstract	iv
Acknowledgements	v
Contents	vi
List of figures	viii
<b>1. Introduction</b>	<b>1</b>
<b>2. Review of literature</b>	<b>6</b>
<b>3. Mathematical Formulation</b>	<b>13</b>
3.1 Introduction .....	13
3.2 Statement of the Problem .....	13
3.3 Details of the Computational Scheme .....	17
3.4 Boundary Conditons .....	20
3.5 Discretization of the equation .....	24
3.6 Pressure Velocity Iteration .....	25
3.7 Solution of Energy Equation .....	30
3.8 Stability Creteria .....	31
<b>4. Results and Discussions</b>	<b>34</b>
4.1 Validation Study .....	34
4.2 Mean Velocity result .....	40
4.3 Reynolds Stresses Profile .....	46
4.4 Average Pressure Distribution .....	52
4.5 Nusselt Number Distribution .....	58
4.6 Power Spectra .....	58



4.7 Reynolds number effect .....	67
4.8 Instantaneous flow fields .....	67
<b>5. Conclusion and Scope for future works</b>	<b>76</b>

## List of figures

1.1	Basic structures of a gas turbine blade .....	2
1.2	Schematics of a flow in a channel with turbulators .....	3
3.1	Schematics of the Computational domain .....	15
3.2	Discretization of three-dimensional domain .....	16
3.3	Three-dimensional Staggered grid showing the locations of the discretized variables .....	16
3.4	Boundary condition and fictitious boundary cells .....	21
3.5	Transient flow MAC algorithm and its variables .....	33
4.1	Time averaged mean Streamwise velocity profile .....	35
4.2	Variation of $fXRe$ along the channel length .....	38
4.3	$fXRe$ variation along the hydrodynamic entrance length for developing flow .....	39
4.4	Nusselt number variation along the Thermal entrance for hydrodynamically Developed flow .....	41
4.5	Variation of time-averaged mean streamwise velocity at different locations in the downstream .....	42
4.6	Variation of time-averaged mean transverse velocity at different locations in the downstream .....	47
4.7	Variation of time-averaged streamwise normal stresses at different locations in the downstream .....	49
4.8	Variation of time-averaged transverse normal stresses at different locations in The downstream .....	53
4.9	Variation of time-averaged shear stresses at different locations in the downstream .....	55
4.10	Average Non-dimensional Pressure Distribution along the length .....	59

4.11	Spanwise average Nusselt number distribution along the length .....	60
4.12	Power Spectra at $Re=2500$ at different locations .....	61
4.13	Variation of time-averaged streamwise normal stresses at different Reynolds number in the downstream .....	64
4.14	Power Spectra at $Re=3500$ .....	66
4.15	Velocity vector plot at the Spanwise midplane at different time-steps.....	68
4.16	Instantaneous Isovorticity plot at the Spanwise midplane .....	70
4.17	Time averaged vorticity plot at Spanwise midplane .....	72
4.18	Velocity Signal at $Re=2500$ .....	73
4.19	Phase plane plot at $Re=2500$ .....	74

# NOMENCLATURE

A	width of the channel
f	frequency of vortex shedding , Hz
h	heat transfer coefficient
H	Height of the channel
K	thermal conductivity of the fluid
Nu	local Nusselt number based on bulk temperature of the fluid
$\overline{Nu}$	Combined Average Nusselt number
p	static pressure
P	nondimensional static pressure
$P'$	pressure correction
Pr	Prandtl number
q	heat flux
Re	Reynolds number, $\rho U_{av} B / \mu$
t	time,sec
T	temperature
u,v,w	streamwise,transverse and spanwise components of velocity respectively
$u',v',w'$	Three components of total velocity fluctuations
$\bar{u}, \bar{v}, \bar{w}$	Time – averaged three components of velocity
$\overline{u'v'}$	Time-averaged shear stress due to velocity fluctuations
$\overline{u'u'}$	Time-averaged streamwise normal stress due to velocity fluctuations
$\overline{v'v'}$	Time-averaged transverse normal stress due to velocity fluctuations

$U, V, W$	axial, normal and spanwise components of velocity (nondimensional)
$U_{av}$	average velocity of fluid at channel inlet
$x^+$	axial coordinate for the hydrodynamic entrance region
$x^*$	axial coordinate for the thermal entrance length
$x, y, z$	streamwise, transverse and spanwise dimension of coordinates
$X, Y, Z$	axial, normal and spanwise coordinates (normalised by $H$ )

### Greek Symbols

$\nu$	kinematics viscosity of fluid, $m^2/sec$
$\theta$	temperature (nondimensional)
$\mu$	Dynamic viscosity of the fluid, $m^2/sec$
$\rho$	Density of the fluid, $kg/m^3$
$\bar{\omega}$	Time – averaged vorticity

### Subscripts

w	wall
b	bulk condition
av	average
$\infty$	inlet condition for the temperature

# CHAPTER 1

## INTRODUCTION

For high thermal efficiency the advanced aeroengines use high temperature gas (1400-1500° C) at the entry of the turbines. Often such temperature is well above the allowable metal temperature. Therefore, highly efficient cooling technologies such as film cooling, impingement cooling, and rib augmented cooling are employed for the turbine blades. In general, film cooling is imposed on the external surface of the blades, while forced cooling is imposed inside the blades by means of cooling passages. To trip the boundary layers for promoting turbulence and thereby enhancing heat transfer, various kinds of turbulators (ribs) are usually provided on the walls of the blade cooling passages.

The rib turbulators is the principal means to enhance heat transfer for internal cooling. These ribs increase the heat transfer in the duct flows by increasing the heat transfer area (fin effect) and by disturbing the laminar sublayer (roughness effect). Fig 1.1(a) shows air entering the rib roughened channel inside the blades and then enters the pin-fin-channel. Since heat is conducted from the pressure and suction surfaces, rib turbulators are cast only on two opposite walls of cooling channel. In Fig 1.1 (b) a cross-section of a blade has been shown. Heat is removed internally from both suction side and pressure side.

The mechanistic model of the flow and the geometry of interest is better represented in Fig 1.2. Due to the symmetry only one half of the channel has been considered. Flow

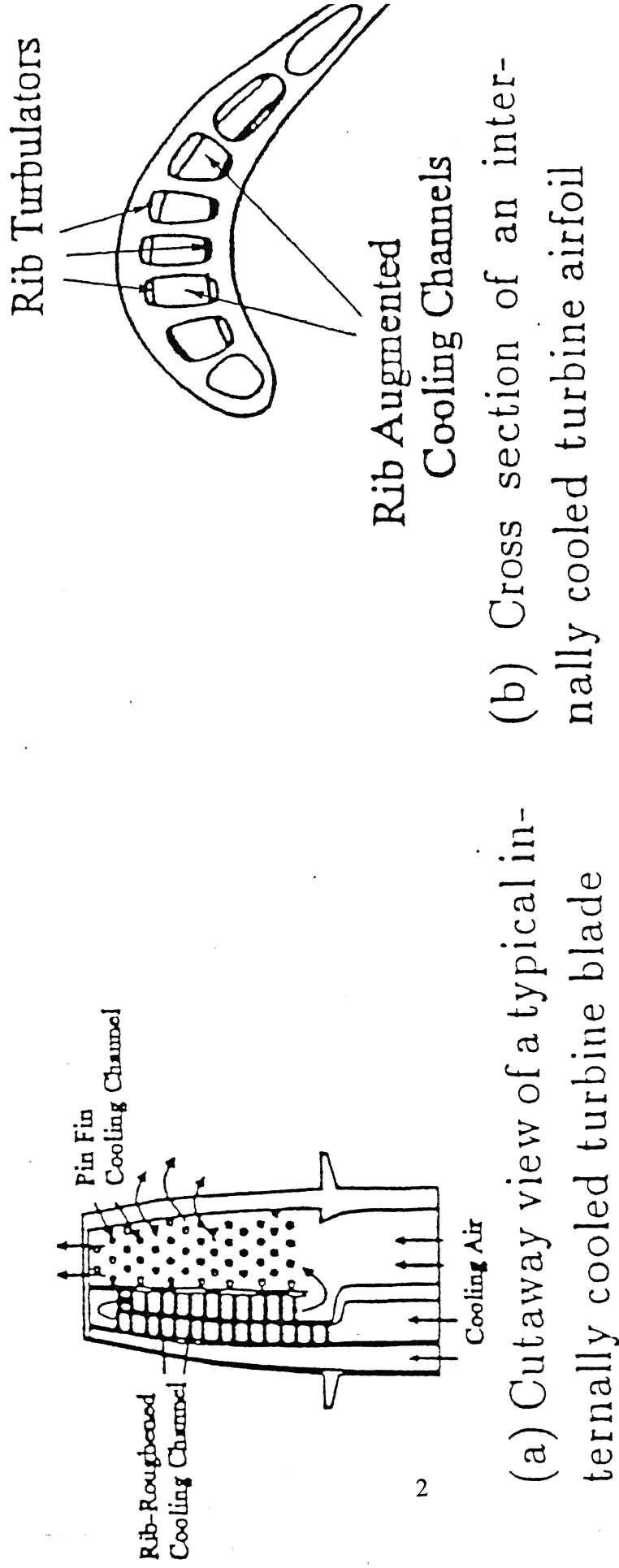


Figure 1.1: Basic structure of a gas turbine blade

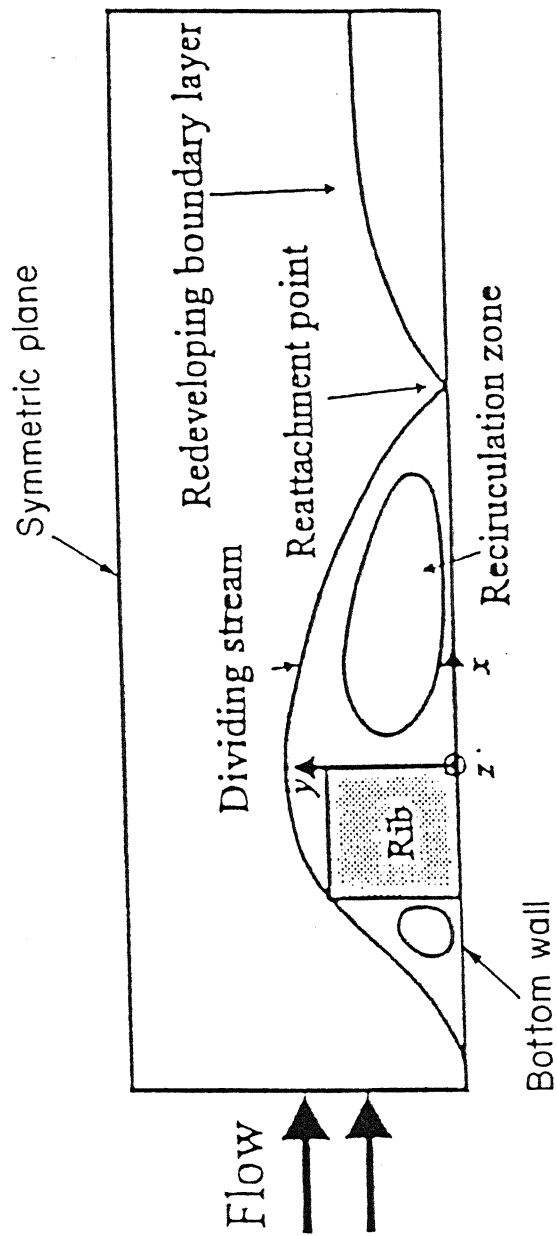


Figure 1.2: Schematics of a flow in a channel with rib turbulator



separates at the leading edge of rib and reattaches at the bottom wall downstream of the rib. A circulating region develops in front of the rib and a large recirculation zone (wake) formed behind the rib. After the reattachment the boundary layer redevelops.

The study of flow past surface mounted rib has been the focus of numerous investigations. These studies has been motivated by the desire to understand the fundamental physics of such flows due to their numerous practical applications, such as the internal coolant channels of gas turbine blades, internally ribbed heat exchangers and in electronic cooling. Research in fields related to vortex generation induced heat transfer enhancement and transition to turbulence has contributed significantly to improved designs and efficiency.

Han et al. (1989) studied the effects of channel aspect ratio and rib angle of attack on the distributions of local heat transfer coefficient and on the friction factor in short rectangular channels of narrow aspect ratio with a pair of rib-roughened walls. The results indicate that narrow-aspect-ratio channels give better heat transfer performance than the wide aspect ratio channel for the constant pumping power.

Durao et al. (1991) investigated the velocity characteristics of the flow around a square cross section cylinder placed near a channel wall. The detailed results of time averaged mean flow properties, turbulence intensities and Reynolds stresses revealed the structural difference of the near wake with and without vortex shedding.

Arnal et al. (1991) studied unsteady flow past a bluff body of square cross section and the effects of this flow on an adjacent wall, which is either fixed or sliding at the bulk fluid velocity.

Acharya et al (1994) obtained detailed Laser Doppler measurements of the flow in the upstream and downstream recirculation regions of a separated duct flow past a wall-mounted, two-dimensional rib and evaluated the ability of the non-linear  $k-\varepsilon$  model to predict the flow behavior.

The present study is aimed at simulating three dimensional flow structures in a duct with a rib- turbulators attached on the bottom wall. The flow structure and temperature fields are to be studied. The effect of flow structure on the performance of the heat transfer is the subject of interest of this thesis.

## **Organization of the thesis**

Subsequent chapters of the present thesis have been organized in the following manner. Chapter 2 reviews the literature related to different aspects of flow and augmented heat transfer in rectangular channels of narrow aspect ratio with rib turbulators. Chapter 3 contains governing equations, different boundary conditions, grid used and details of the numerical techniques. Results and discussions have been discussed in Chapter 4. Chapter 5 summarizes major conclusion of the present work and outlines the scope for future works.

## CHAPTER 2

### Review of Literature

The present chapter deals with a review of relevant literature concerning flow characteristics and augmentation of heat transfer in a rectangular channel with opposite rib roughened walls. A horde of experimental and computational works have been accomplished in related fields in the past due to its numerous practical applications such as the internal coolant channel of gas turbine blades, internally ribbed heat exchangers and in electronic cooling. The objective of this section is to discuss those articles which bring out the salient features of flow and heat transfer mechanism concerning the present work. The review helps in suggesting further investigations that should be taken up in order to address some of the objectives enumerated in the earlier chapter.

Many reserchers in the past three decades tried to develop numerical schemes to solve the incompressible Navier-Stokes equations in three dimension. The main difficulty in incompressible flow simulation arises from the absence of any explicit equation for the pressure and due to the nature of spatial coupling of the pressure and the velocity. Harlow and Welch (1965) used staggered grid for the dependent variables in their well known MAC (Marker and Cell) method. The MAC method of Harlow and Welch is one of the earliest and widely used explicit methods for solving the complete Navier-Stokes equations. A related technique was developed by Chorin (1967) which involves simultaneous iteration of pressure and velocity components. Vicelli (1971) has shown

that the two methods are equivalent. The original version of the MAC method was modified by Hirt and Cook (1972) for the application to free surface flows. The MAC method has been extensively used by many reserchers to solve the flow field of complex geometries and it has been succesful to simulate highly unsteady turbulent flows. It has been experienced that the MAC method has stability restrictions on the time step which slows down the calculations for steady flows considerably. Since implicit methods have no such restrictions, they are more attractive. Patankar and Spalding (1972) have introduced an efficient method known as SIMPLE (Semi-Implicit Method for Pressure Linked Equations). This method is based on a finite-volume discretisation of the governing equations on a staggered grid. In order to improve the convergence involved in the pressure-velocity coupling, several variants of SIMPLE algorithm have also been developed.

Patankar et al. (1977) studied fully developed flow and heat transfer in ducts having streamwise periodic variations of cross-sectional area due to transverse plate array. The concept and solution procedure for the periodic fully developed regime was applied to a heat exchanger configuration consisting of successive ranks of isothermal plate segments placed transverse to the mainflow direction. The computed laminar flow fields are found to be characterized by strong blockage effects and massive recirculation zones. There was rapid turning of the flow in response to the blockage imposed by the front face of the plates. The fully developed Nusselt number was found to be much higher than conventional laminar duct flows and show a marked dependence on the Reynolds number.

The length of recirculation region past a two dimensional obstacle placed at the surface was investigated experimentally with a single hot wire by Bergeles et al. (1983). The results show that in upstream of the obstacle the length of the main recirculation region remains unchanged with obstacle width and equal to  $0.85H$ , however the downstream length of the recirculating is a strong function of the width and changes almost linearly from 11 obstacle height for  $W/H=1.0$  to 3 for  $W/H$  greater than four. Vogel et al. (1985)

studied the combined heat transfer and fluid dynamics measurements in a separated and reattaching boundary layer with emphasis on the near wall region. A constant heat flux surface behind a single sided expansion was used to obtain, Stanton number profiles as a function of Reynolds number and boundary layer thickness at separation. Fluctuating skin-friction and temperature profiles demonstrated the importance of the near-wall region in controlling the heat transfer rate. The fluctuating skin friction controls the heat transfer rate near reattachment, while the conventional Reynolds analogy applied in the redeveloping boundary layer beginning two or three step heights downstream of reattachment.

Ghadder et al. (1986) investigated the incompressible moderate Reynolds numbers flow in periodically grooved channels by direct numerical simulation using the spectral element method. For Reynolds number less than a critical value,  $Re_c$  the flow is found to approach a stable steady state, comprising an outer channel flow and a weak recirculating vortex in the groove. The instability of the linear mode for  $Re > Re_c$  results in self-sustained flow oscillations, which again resemble Tollmien-Schlichting modes driven by an unstable groove vortex street.

Patankar et al. (1987) studied fluid flow and heat transfer in two-dimensional finned passages for constant property laminar flow. The flow was characterized by large recirculation zones and significant flow distortion. A substantial increase in heat transfer was observed especially for high Prandtl number fluids. However, the increase in friction factor was an order of magnitude higher than increase in heat transfer. Han et al. (1988) studied the effect of the channel aspect ratio on the distribution of the local heat transfer coefficient in rectangular channels with two opposite rib-roughened walls. The results indicated that local Nusselt number on the ribbed wall is two to three times higher than the four-sided smooth channel values. The results indicate that the narrow aspect-ratio channels give better heat transfer performance than wide aspect-ratio channels for a constant pumping power.

Antonious et al. (1988) made velocity and turbulence measurements for the region after reattachment behind a two-dimensional surface-mounted prism of varying length. Longitudinal integral time and length scale was estimated through autocorrelations. The reattachment on the top of the prism, due to its increased length was found to influence the characteristics of the developing boundary layer. In this case the shear layer originating from the upstream edge of the prism splits twice at reattachment point on top and behind the prism and the integral length scales of the turbulent eddies are found to be smaller due to splitting. The flow pattern and heat transfer enhancement in supercritical grooved-channel and communicating-channel was numerically investigated by Amon and Mikic (1990). For Reynolds number above the critical one the flow exhibit laminar self-sustained oscillation at the plane channel Tollmien-Schlichting frequency. These ordered very well mixed flows were found require significantly less pumping power than the random fluctuating flows to achieve the same transport rates.

Acharya et al. (1990) made experimental study to examine the effect of subharmonic forcing on a, reattaching shear layer behind a rib in a duct flow. They observed the merging of the vortices which leads to the enhancement in entrainment and shear-layer growth. Phase averaged pressure was shown to be related to the passage of vortices. The pressure spectra indicate that the initial vortex dynamics dictate the pressure field. Garimella et al. (1991) studied flow visualization and measurements of velocity and turbulence intensity using Laser Doppler Velocimetry to investigate separation and reattachment process in the flow over an array of protruding elements mounted on the bottom wall of a rectangular water channel. The concepts of an array shear layer was introduced to demarcate the region of influence over which the resistance of the array retards the flow. The reattachment length downstream of the element varies from 4 to 1.5 element height, decreasing both with an increase in Reynolds number and a decrease in channel height. Durao et al. (1991) made LDV measurements of the flow around a square cross-section cylinder placed near a channel wall. The detailed results of the time averaged mean flow properties, turbulence intensities and Reynolds stresses revealed the structural difference of the near wake with and without vortex shedding. The magnitude

of the time averaged normal and shear stresses decrease markedly with the proximity of the square cross section cylinder to the wall.

Arnal et al. (1991) studied unsteady flow past a bluff body of square cross section and the effect of an adjacent wall, which is either fixed or sliding at the bulk velocity on the flow field. Results indicate that the presence of a wall and the streamwise shear induced by it strongly affects the stability of the flow and the type of vortex shedding. In fact, the geometry and spatial boundary conditions influence the vortex shedding and the type of wake that are observed to a greater extent than the Reynolds number. Comparison with results from the freestream simulation show that the presence of a wall stabilises the flow and increases the critical Reynolds number at which the flow becomes unsteady. The presence of wall was also shown to reduce the Strouhal number at which vortex shedding occurred. A particularly interesting finding of the current study is that the presence of a wall which slides at the free stream velocity results in vortex shedding which is strongly periodic. Amon et al. (1992) made numerical and experimental investigation of flow field and thermal phenomena in communicating channels to gain insight into the operation of compact heat exchanger with interrupted surfaces. The mixing is found to be significantly enhanced as a result of travelling waves at relatively low Reynolds number, inducing self-sustained oscillatory flows.

Myrum et al. (1992) studied the vortex generation induced heat transfer augmentation past a rib in a heated duct airflow. The Local and average Nusselt number results were obtained for a circular rod positioned either immediately above or just downstream of the rib. The enhancement in Nusselt number was found to be the function of flow rate, diameter of rod and the rib spacing. The heat and momentum transport in self-sustained oscillatory viscous flow of communicating channel was investigated numerically by Majumdar et al. (1992) using the Spectral element method. Above a critical Reynolds number the flow was found to bifurcate into a time-periodic, self sustained oscillatory state and the correlation between the time and space averaged Nusselt and Reynolds number was obtained.

Biswas et al. (1992) studied numerically the structure of flow and heat transfer characteristics in a rectangular channel with a built in delta wing protruding from the bottom wall. Augmentation of heat transfer between the flowing fluid and the channel wall was found. The combined spanwise average Nusselt number showed increase as large as 34% even at the exit of a long channel at an angle of attack of  $26^\circ$ . The vortex generator's angle of attack and Reynolds number were found to affect heat transfer and skin friction significantly. Acharya et al. (1994) studied the ability of the non-linear  $k - \varepsilon$  turbulence model to predict the duct flow past a wall mounted two-dimensional rib and compared the results with standard  $k - \varepsilon$  turbulence model and observed that improved predictions of the streamwise turbulent intensity and the mean streamwise velocities near the high-speed edge of separated shear layer and the flow downstream of reattachment were obtained with nonlinear model.

Prakash et al. (1995) predicted numerically the turbulent flow and heat transfer in ribbed rectangular duct with and without rotation. Due to the Coriolis induced secondary flow, rotation was found to enhance heat transfer from the trailing and the sidewalls, while decrease the heat transfer from the leading face. Relative to the corresponding stationary case, the effect of rotation was found to be less for a ribbed channel as compared to a smooth channel Hwang (1998) compared fully developed heat transfer and friction characteristics in rectangular duct with one wall roughened by slit and solid ribs. Because of the greater turbulence mixing effects, the slit-ribbed geometry was found to display higher floor heat transfer than the solid rib.

Balachandar et al. (1998) made a detailed analysis of experimental and numerical results of flow and heat transfer in offset strip fin heat exchangers. Surface average heat transfer, pressure drop, local Nusselt number and skin friction coefficient on the fin surface were compared. The instantaneous flow structure and the local time averaged velocity profile were presented for a range of Reynolds number. The results indicated that the study of the boundary layer development, flow separation and reattachment, wake formation and vortex shedding are important in designing complex geometry. Chiang et al. (1999) studied a laminar flow evolving into a larger channel over a three-dimensional backward



facing step for a range of Reynolds number. The effect of span width on the flow reversal and the effect of the end wall on the overall flow structure is significant. The computed surface streaking patterns gave a good indication of the extent of the reverse-flow zone.

## **CHAPTER 3**

### **MATHEMATICAL FORMULATION**

#### **3.1 Introduction**

The study of flow over a surface mounted rib has attracted many researchers due to its various practical applications such as the internal coolant channel of gas turbine blades, internally ribbed heat exchangers and in electronic cooling. Research in the related field has helped in improving the design and efficiency of these equipments significantly. The improved numerical model and solution technique help in quickly analysing the flow configurations with all its complexities. Present work, is a modest attempt at studying the features of flow and heat transfer about a three dimensional rectangular rib placed at the bottom channel wall.

#### **3.2 STATEMENT OF THE PROBLEM**

##### **3.2.1 Governing Equation**

Computation is performed for incompressible flow in a rectangular channel with a pair of symmetrical rectangular ribs placed at the channel walls. The geometry of the present

problem is presented in Fig 3.1. Flow field is simulated by the solution of Navier –Stokes equations. The Navier-Stokes equations are capable of describing all the nuances of a fluid flow phenomena. Complete Navier Stokes equation are solved for the present problem. The governing equation for incompressible three dimensional laminar flow in Cartesian coordinates are written as

$$\frac{\partial U}{\partial X} + \frac{\partial V}{\partial Y} + \frac{\partial W}{\partial Z} = 0 \quad (3.1)$$

$$\frac{\partial U}{\partial t} + \frac{\partial U^2}{\partial X} + \frac{\partial UV}{\partial Y} + \frac{\partial UW}{\partial Z} = -\frac{\partial P}{\partial X} + \frac{1}{\text{Re}} \left\{ \frac{\partial^2 U}{\partial X^2} + \frac{\partial^2 U}{\partial Y^2} + \frac{\partial^2 U}{\partial Z^2} \right\} \quad (3.2)$$

$$\frac{\partial V}{\partial t} + \frac{\partial VW}{\partial X} + \frac{\partial V^2}{\partial Y} + \frac{\partial VW}{\partial Z} = -\frac{\partial P}{\partial Y} + \frac{1}{\text{Re}} \left\{ \frac{\partial^2 V}{\partial X^2} + \frac{\partial^2 V}{\partial Y^2} + \frac{\partial^2 V}{\partial Z^2} \right\} \quad (3.3)$$

$$\frac{\partial W}{\partial t} + \frac{\partial UW}{\partial X} + \frac{\partial VW}{\partial Y} + \frac{\partial W^2}{\partial Z} = -\frac{\partial P}{\partial Z} + \frac{1}{\text{Re}} \left\{ \frac{\partial^2 W}{\partial X^2} + \frac{\partial^2 W}{\partial Y^2} + \frac{\partial^2 W}{\partial Z^2} \right\} \quad (3.4)$$

$$\frac{\partial \theta}{\partial t} + \frac{\partial (U\theta)}{\partial X} + \frac{\partial (V\theta)}{\partial Y} + \frac{\partial (W\theta)}{\partial Z} = \frac{1}{\text{Pe}} \nabla^2 \theta \quad (3.5)$$

In the above equations the velocities have been non-dimensionalized with respect to free stream velocity  $U_\infty$  and all the lengths are non-dimensionalized using the channel height  $H$ . The pressure is non-dimensionalized with respect to  $\rho U_\infty^2$ . No assumption about the relative magnitude of the different terms has been made in this study. Temperature is nondimensionalised as  $\theta = \frac{T - T_\infty}{T_w - T_\infty}$  where  $T_w$  is the wall temperature.

### 3.2.2 GRID

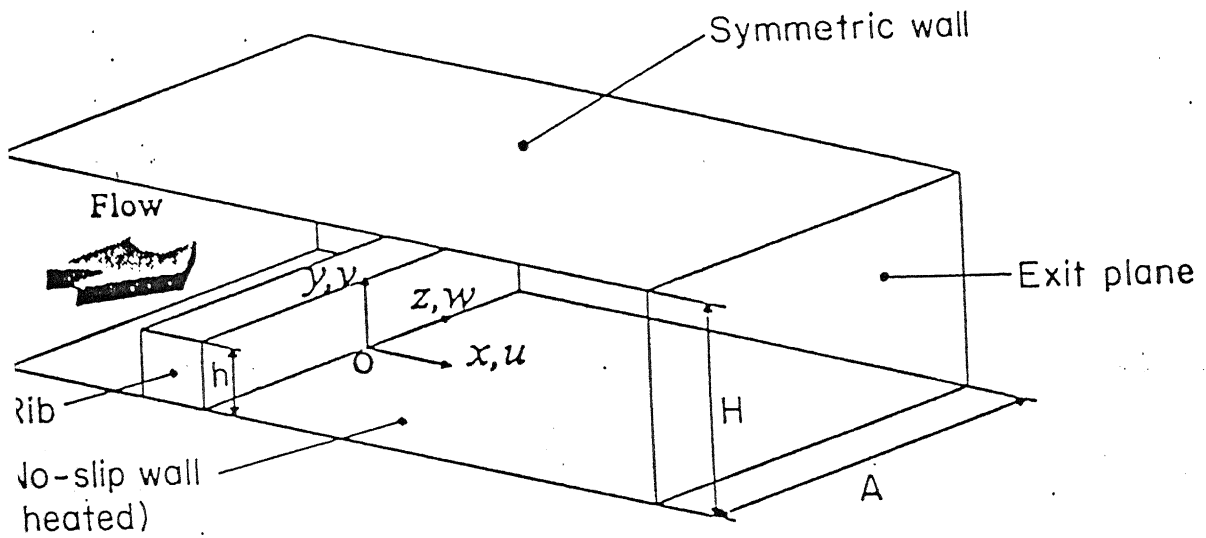


Figure 3.1 Computational domain

NON DIMENSIONAL PARAMETERS

LENGTH - 6.75

WIDTH - 5

HEIGHT - 1

HEIGHT OF OBSTACLE - 0.1

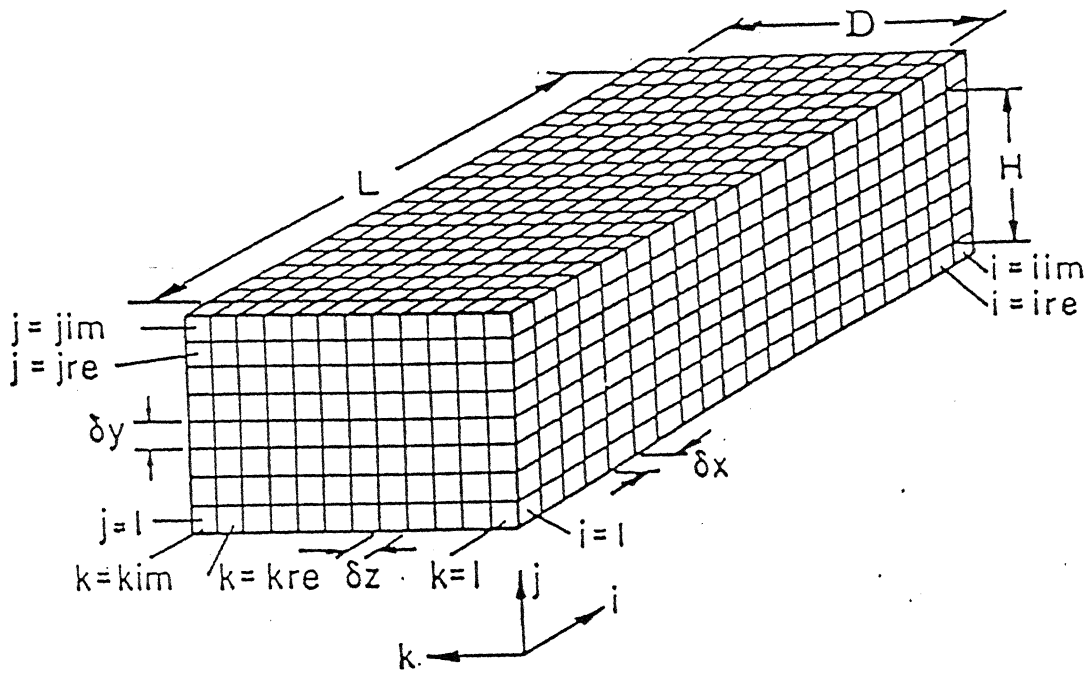


Fig 3.2 Discretization of a three-dimensional domain

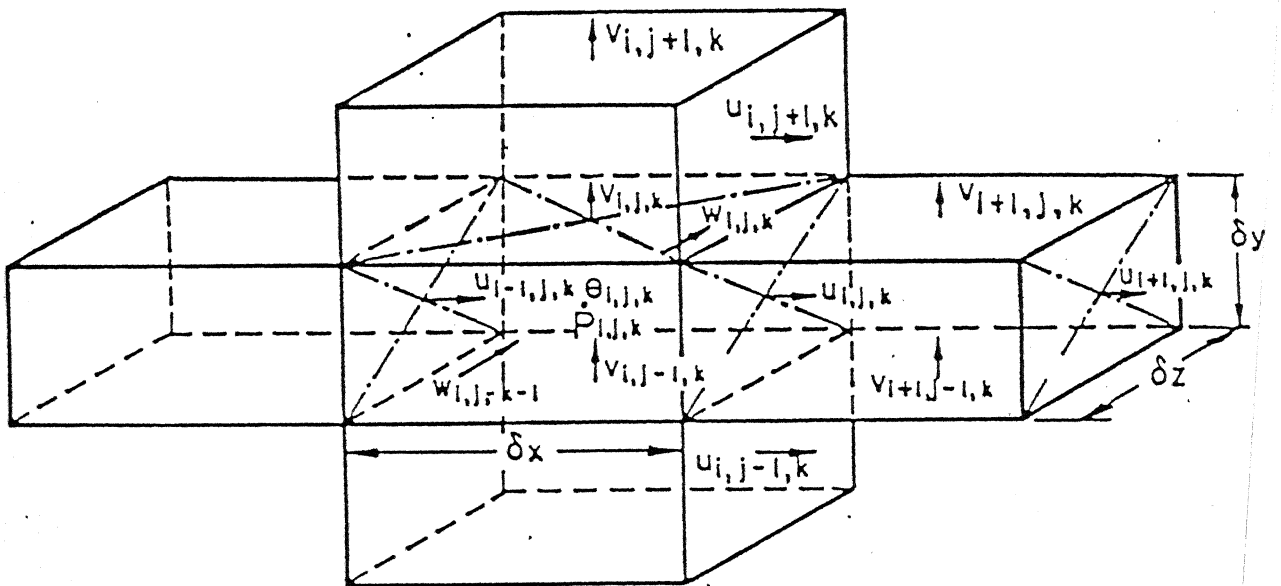


Fig 3.3 Three-dimensional staggered grid showing the locations of the discretized variables

For the computational work a grid-mesh is generated which divides the domain of interest into a number of cells. The choice of grid system is dependent on the type of geometry involved in the computation. The computational domain is divided into a number of rectangular cells of edge length  $\partial X$ ,  $\partial Y$  and  $\partial Z$  along the X, Y and Z directions respectively (Fig 3.2). Cells are denoted by an index (i,j,k) implying cell number as counted from the origin in X,Y and Z directions respectively. Staggered grid arrangement is used (Fig 3.3). The velocities are defined at the center of the cell-faces to which they are normal. The pressure and temperature are defined at the centre of the cell.

### **3.3 Details of Computational Scheme**

#### **3.3.1 Marker –and –Cell Method**

The nondimensional continuity, momentum and energy equations in their conservative form, are solved by using a modified version of Marker and Cell (MAC) algorithm. The original version of MAC due to Harlow and Welch (1965) was modified by Hirt and Cook (1972). In the original MAC method, the pressure field was obtained by directly solving the Poisson equation for pressure, whereas, in the modified MAC version, pressure values are calculated implicitly from continuity equation by a pressure velocity iteration process. A related technique developed by Chorin (1967) in the context of artificial compressibility method involved a simultaneous iteration on pressure and velocity components. Viegelli (1971) has shown that the two methods as applied to the MAC algorithm are equivalent.

### **Computational Scheme**

MAC is a semi-implicit scheme for solving complete Navier –Stokes equations where the advancement of the velocity components in the time direction is obtained explicitly by calculating acceleration due to the convection, diffusion, and the pressure gradient. Thus

after obtaining a provisional velocity field for the next from the previous time levels time step, the continuity equation is solved implicitly to correct the provisional velocity field.

The complete Navier-Stokes equations are elliptic in space and parabolic in time. Hence a time- marching scheme is necessary to obtain the transient flow solutions . Since the equations are elliptic in space, boundary conditions need to be imposed on all the confining boundaries, even at the outlet. To start the computation, guess fields of velocity, pressure and temperature are assumed. From the guessed velocity and pressure fields, the corrected velocity and pressure fields are obtained by pressure velocity iteration through the continuity equation. Convergence of this iteration process ensures a divergence free velocity field for the initial time step.

Subsequently the corrected pressure velocity fields are used to calculate the velocity field for the next time step by solving the Navier Stokes equations . The time step  $\delta t$  for the advancement of the velocities is governed by the stability criteria which is discussed in a subsequent section. The satisfaction of continuity equation is achieved by adjusting the pressure as well as velocities in each cell through an iterative process, which as mentioned earlier, is equivalent to the solution of Poissons equation for pressure. Details of pressure velocity iteration procedure will be discussed in the following section. Thus starting from initial guess fields, the solution advances in the time direction until a steady or periodic solution is obtained. The solution of the energy equation is however, relatively simple. After a steady or unsteady velocity field is obtained, the energy equation is solved by the Successive Over Relaxation (SOR) technique.

## **Boundary Conditions**

The boundary conditions of interest in the investigation are

Bottom Plate :

$$U = V = W = 0$$

Top Plate :

$$\frac{\partial U}{\partial Y} = V = \frac{\partial W}{\partial Y} = 0$$

Side Plate :

$$\frac{\partial U}{\partial Z} = \frac{\partial V}{\partial Z} = W = 0$$

Channel Inlet :

$$U = U(Y), V = W = 0$$

Channel exit

There is no unique prescription for outflow conditions. The idea is to have such conditions which do not affect the flow in the upstream. The second or higher order derivatives of all the velocity components in the streamwise direction are put to zero.

$$\frac{\partial^2 U}{\partial X^2} = \frac{\partial^2 V}{\partial X^2} = \frac{\partial^2 W}{\partial X^2} = 0 \quad (3.6)$$

Obstacle :

No-slip boundary conditions are used for the velocities on the obstacle.

## Numerical Boundary Conditions



We have discussed the boundary conditions of symbolic form. It is necessary to discuss the implementation technique of the boundary condition in the solution code. The boundary conditions are imposed by setting the appropriate velocities in the fictitious (or imaginary) cells surrounding the physical domain.

## Boundary Conditions for Confining walls

The governing differential equations are elliptic in space and parabolic in time. We need the boundary conditions for all the confining surfaces. Since the confining walls at the top and bottom are rigid for the present computation, both the normal and the tangential components of velocity on the wall must be zero. With reference to Fig.3.4, we can write (for the bottom of the computational domain)

$$\left. \begin{aligned} U_{i,1,k} &= -U_{i,2,k} \\ V_{i,1,k} &= 0 \\ W_{i,1,k} &= -W_{i,2,k} \end{aligned} \right\} \begin{array}{l} \text{for } i = 2 \text{ to } ire \\ \text{for } k = 2 \text{ to } kre \end{array} \quad (3.7)$$

Similarly, for Symmetric wall the boundary conditions become

$$\left. \begin{aligned} U_{i,1,k} &= U_{i,2,k} \\ V_{i,j,k} &= 0 \\ W_{i,j,k} &= W_{i,2,k} \end{aligned} \right\} \begin{array}{l} \text{for } i = 2 \text{ to } ire \\ \text{for } k = 2 \text{ to } kre \end{array} \quad (3.8)$$

Similarly, for the free slip right wall, the boundary conditions become

$$\left. \begin{aligned} U_{i,j,1} &= U_{i,j,2} \\ V_{i,j,1} &= V_{i,j,2} \\ W_{i,j,1} &= 0 \end{aligned} \right\} \begin{array}{l} \text{for } i = 2 \text{ to } ire \\ \text{for } j = 2 \text{ to } jre \end{array} \quad (3.9)$$

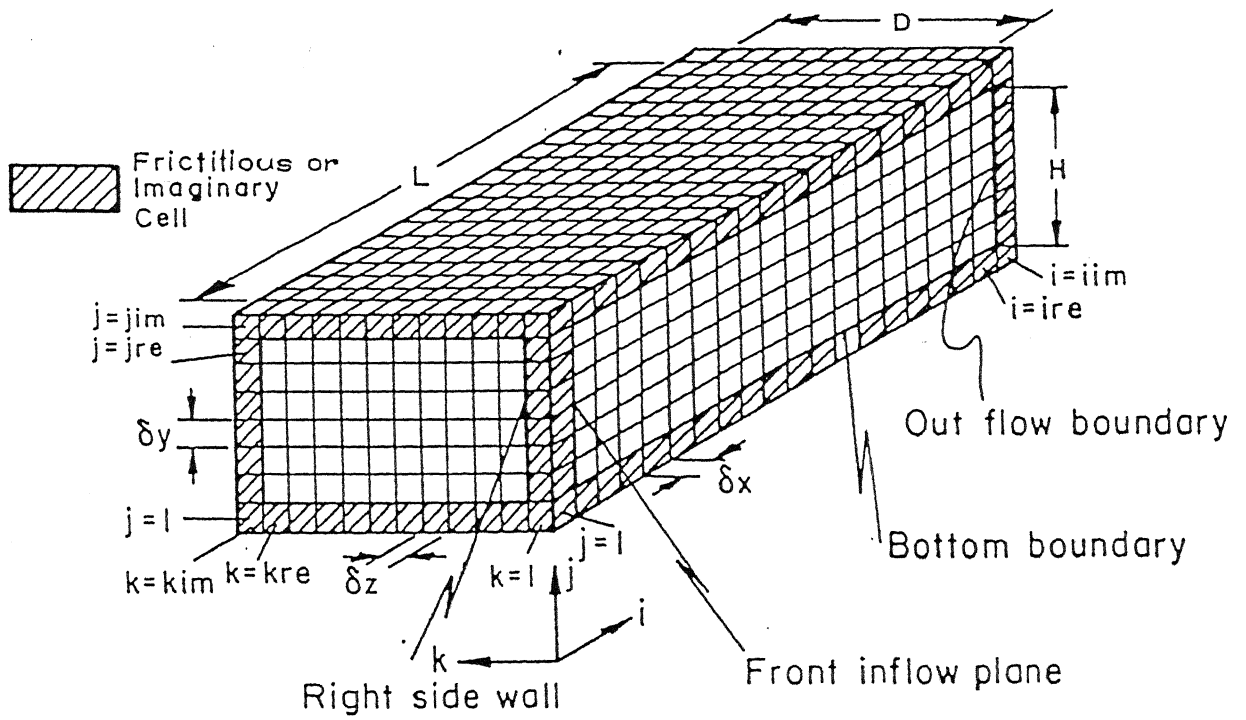


Figure 3.4. Discretization of a three-dimensional domain

### 3.4.1 Boundary condition for the Obstacle

In order to implement the kinematic boundary conditions on the obstacle, the velocity point which are in the domain of the obstacle are set equal to zero. The implementation is explained with the help of a three dimensional flow simulation. Application for a two dimensional case is straight forward. Implementation of the no-slip condition for V- and W-components of velocity along the transverse direction, U-component of velocity along the direction of flow need some manipulations. With reference to figure 3.1 the boundary conditions is prescribed in a manner such that the points falling on the obstacle surface in the x direction is from ii2 to ii3, in the y direction from 1 to jj1 and in the z direction from 1 to kim, following which the boundary condition is defined as

$$U_{i,j,k} = -U_{i,j,k-1} \quad \text{for } i = ii2-1 \text{ to } ii3 \quad \text{at } k=1 \quad (3.12)$$

$$U_{i,j,k} = -U_{i,j,k-1} \quad \text{for } i = ii2-1 \text{ to } ii3 \quad \text{at } k=kim \quad (3.13)$$

similarly, for the V-component of velocity, we have

The front plane (inlet plane) is to be provided with the inflow boundary condition. The normal velocity components are set to zero and a uniform or parabolic axial velocity may be deployed. Hence, with reference to Fig.3.4 we can use

$$\left. \begin{aligned} W_{1,j,k} &= -W_{2,j,k} \\ V_{1,j,k} &= -V_{2,j,k} \\ U_{1,j,k} &= 1.0 \end{aligned} \right\} \begin{array}{l} \text{for } j = 2 \text{ to } ire \\ \text{for } k = 2 \text{ to } kre \end{array} \quad (3.10)$$

$$\text{or, } U_{1,j,k} = 1.5 \left[ 1 - \left\{ \frac{j_m - 1}{j_m} \right\}^2 \right]$$

where  $j_m$  is the horizontal mid-plane.

Continuative or outflow boundaries always pose a problem for low-speed calculations, because whatever prescription is chosen it can effect the entire flow field upstream. We should follow a prescription that allows fluid to flow out of the computational domain with a minimum of upstream influence. In our present computation, the second derivative of the dependent variables with respect to flow direction are set to zero to ensure smooth transition through the outlet boundary. These can be implemented in the following way:

$$\left. \begin{aligned} U_{i+1,j,k} &= 2U_{i,j,k} - U_{i-1,j,k} \\ V_{i+1,j,k} &= 2V_{i,j,k} - V_{i-1,j,k} \\ W_{i+1,j,k} &= 2W_{i,j,k} - W_{i-1,j,k} \end{aligned} \right\} \begin{array}{l} \text{for } j = 2 \text{ to } jre \\ \text{for } k = 2 \text{ to } kre \\ \text{at } i = iim - 2 \end{array} \quad (3.11)$$

The governing equations and the boundary conditions discussed so far are described for a three dimensional problem. The two dimensional problem is a subset of the three dimensional problem and the implementation is straightforward.

$$V_{i,j,k} = -V_{i,j,k-1} \quad \text{for } i=ii2 \text{ to } ii3 \quad \text{at } k=1 \quad (3.14)$$

$$V_{i,j,k} = -V_{i,j,k+1} \quad \text{for } i=ii2 \text{ to } ii3 \quad \text{at } k=kim \quad (3.15)$$

$$V_{i,j,k} = -V_{i-1,j,k} \quad \text{for } k=1,kim \quad \text{at } i=ii2 \quad (3.16)$$

$$V_{i,j,k} = -V_{i+1,j,k} \quad \text{for } k=1,kim \quad \text{at } i=ii3 \quad (3.17)$$

finally , for the W-component of velocity, one can have

$$W_{i,j,k} = -W_{i-1,j,k} \quad \text{for } k=2 \text{ to } kim \quad \text{at } i=ii2 \quad (3.18)$$

$$W_{i,j,k} = -W_{i+1,j,k} \quad \text{for } k=2 \text{ to } kim \quad \text{at } i=ii3 \quad (3.19)$$

### 3.4.2 Temperature boundary condition

The uniform wall temperature boundary condition is imposed on the channel walls and the surface of the obstacle. With reference to Fig 3.1 the temperature boundary condition are prescribed as

- On the obstacle surface

The obstacle surfaces are assumed to be at the same common wall temperature  $T_w$ . This is implemented by putting

$$\theta_{wall} = 1 \quad (3.20)$$

- Confining Boundary of the domain

The boundary condition on the channel wall is imposed in the following manner, since the temperature is defined at the centre of the cell outside the boundary .

$$\theta(i,j,k) = 2 - \theta(i,j+1,k) \quad \forall i,k \text{ and } j=1 \quad (3.21)$$

At the midplane of the channel symmetric boundary condition is applied by putting

$$\theta(i, j, k) = \theta(i, j-1, k) \quad \forall i, k \text{ and } j=j_{\text{im}} \quad (3.22)$$

- inflow

The temperature at entry is specified by putting a constant value

$$\theta = 1 \quad \forall j, k \text{ and } i=1 \quad (3.23)$$

- The exit boundary condition is specified by putting

$$\frac{\partial^2 \theta}{\partial X^2} = 0 \quad \forall j, k \text{ and } i=i_{\text{im}} \quad (3.24)$$

### 3.5 Discretization of the equation

Because of staggered grid arrangement (Fig.3.3) the velocities are not defined at the nodal points. Whenever required, the velocities at the nodal points are calculated by interpolation of neighbouring velocities. As an example, we can write  $U_{i-1/2, k} = 0.5$

$(U_{i-1, j, k} + U_{i, j, k})$ , but where a product or square of such quality appears, it is customary to interpolate first and then the product to be taken.

For any cell, the discretization of the continuity equation is given by

$$U_{i, j, k} = \frac{U_{i, j, k} - U_{i-1, j, k}}{\delta X} + \frac{V_{i, j, k} - V_{i, j-1, k}}{\delta Y} + \frac{W_{i, j, k} - W_{i, j, k-1}}{\delta Z} \quad (3.25)$$

The discretization of the temporal derivatives (3.1) to (3.4) is done by a forward differencing

$$\frac{\partial U}{\partial t} = \frac{U_{i,j,k}^{n+1} - U_{i,j,k}^n}{\delta t} \quad (3.26)$$

The convective terms of the momentum equations are discretized by a weighted average scheme which combines the upwind and central differencing to achieve the stability of upwind and formal accuracy of the central differencing (Hirt, Nichols and Romero, 1975).

The discretization of one of the convective terms is shown below:

$$\begin{aligned} \frac{\partial(UV)}{\partial Y} = & \frac{1}{4\delta Y} [(V_{i,j,k} + V_{i+1,j,k})(U_{i,j,k} + U_{i,j+1,k}) \\ & + \alpha |(V_{i,j,k} + V_{i+1,j,k})|(U_{i,j,k} - U_{i,j+1,k}) \\ & - (V_{i,j-1,k} + V_{i+1,j-1,k})(U_{i,j-1,k} + U_{i,j,k}) \\ & - \alpha |(V_{i,j-1,k} - V_{i+1,j-1,k})|(U_{i,j-1,k} - U_{i,j,k})] \end{aligned} \quad (3.27)$$

The factor  $\alpha$  determines the relative weighted of the central and upwind differencing.  $\alpha = 0$  gives simple a central differencing and  $\alpha = 1$  leads to a second upwind differencing. Temporal derivatives are discretized using second order differencing

$$\frac{\partial U}{\partial t} = (U_{i,j,k}^{n+1} - U_{i,j,k}^n) / \delta t \quad (3.28)$$

Diffusion terms are discretized using second order differencing.

$$\frac{\partial^2 U}{\partial X^2} = \frac{1}{\delta X^2} [U_{i+1,j,k} - 2U_{i,j,k} + U_{i-1,j,k}] \quad (3.29)$$

### 3.6 Pressure Velocity Iteration

As there is no pressure boundary condition the solution of Poisson equation is accomplished in an iterative manner. In the original MAC method the Poisons equation was solved for pressure. The modification due to Hirt and Cook (1972) enables one to solve the Poisons

equation in such a way that the velocity and pressure fields are correct and satisfy the governing equations and the velocity boundary are satisfied.

The velocities are advanced explicitly from the momentum equation if the velocities and pressure are known at any time step by calculating the accelerations due to advection, diffusion and pressure gradients. But these values are not necessarily the ones to give a meaningful solution if there is any non-zero value of divergence. Pressure are correct if they are accompanied by zero divergence. The pressure have to be corrected such that there is no accumulation or annihilation of mass anywhere in the domain. Corrections to pressures are applied in an iterative manner as described by Hirt and Cook (1972) which as mentioned earlier is equivalent to the solution of a Poisons equation for pressure.

The method of pressure-velocity correction iteration is as follows. The relationship between the explicitly advanced velocity components at the  $(n+1)^{th}$  time level and that at the previous  $(n)^{th}$  time level can be put as

$$\tilde{U}_{i,j,k}^{n+1} = U_{i,j,k}^n + \left( \frac{\delta t}{\delta X} \right) (P_{i,j,k}^n - P_{i+1,j,k}^n) \delta t (RESIDU)_{i,j,k}^n \quad (3.30)$$

Where  $[RESIDU]_{i,j,k}^n$  is the value of

$$\left[ -\frac{\partial U^2}{\partial X} - \frac{\partial UY}{\partial Y} - \frac{\partial UW}{\partial Z} + \frac{\nabla^2 U}{Re} \right] \quad (3.31)$$

at the  $(i,j,k)$  cell evaluated with the velocity values at the  $n^{th}$  time step. On the other hand, the corrected velocity components, which are still unknown, are, related to the correct pressure (unknown) in the manner.

$$U_{i,j,k}^{n+1} = U_{i,j,k}^n + \left( \frac{\delta t}{\delta X} \right) (P_{i,j,k}^{n+1} - P_{i+1,j,k}^{n+1}) + \delta t [RESIDU]_{i,j,k}^n \quad (3.32)$$

From equations 3.31 and 3.32 one can write

$$U_{i,j,k}^{n+1} - \tilde{U}_{i,j,k}^{n+1} = \left( \frac{\delta t}{\delta X} \right) (P'_{i,j,k} - P'_{i+1,j,k}) \quad (3.33)$$

Where  $P'_{i,j,k} = P_{i,j,k}^{n+1} - P_{i,j,k}^n$

Neither  $\partial P'_{i,j,k}$  nor  $U_{i,j,k}^{n+1}$  are explicitly known at this stage so that one can be calculated with the help of the other. Calculations are done in an iterative cycle and we can write

$$U_{i,j,k}^{n+1} \longrightarrow \tilde{U}_{i,j,k}^{n+1} - \left( \frac{\delta t}{\delta X} \right) (P'_{i,j,k} - P'_{i+1,j,k}) \quad (3.34)$$

In the similar manner the other velocities can be written as

$$U_{i-1,j,k}^{n+1} \longrightarrow \tilde{U}_{i,j,k}^{n+1} - \left( \frac{\delta t}{\delta X} \right) (P'_{i,j,k} - P'_{i-1,j,k}) \quad (3.35)$$

$$V_{i,j,k}^{n+1} \longrightarrow \tilde{V}_{i,j,k}^{n+1} - \left( \frac{\delta t}{\delta Y} \right) (P'_{i,j,k} - P'_{i,j+1,k}) \quad (3.36)$$

$$U_{i-1,j,k}^{n+1} \longrightarrow \tilde{U}_{i,j,k}^{n+1} - \left( \frac{\delta t}{\delta X} \right) (P'_{i,j,k} - P'_{i-1,j,k}) \quad (3.37)$$

$$W_{i-1,j,k}^{n+1} \longrightarrow \tilde{W}_{i,j,k}^{n+1} - \left( \frac{\delta t}{\delta Z} \right) (P'_{i,j,k} - P'_{i,j,k+1}) \quad (3.38)$$

$$W_{i,j,k-1}^{n+1} \longrightarrow \tilde{W}_{i,j,k}^{n+1} - \left( \frac{\delta t}{\delta Z} \right) (P'_{i,j,k} - P'_{i,j,k-1}) \quad (3.39)$$



The correction is done through continuity equation. Plugging in the relationship 3.34 to 3.39 into the continuity equation (3.25) we get,

$$\begin{aligned}
& \left[ \frac{U_{i,j,k}^{n+1} - U_{i-1,j,k}^{n+1}}{\delta X} + \frac{V_{i,j,k}^{n+1} - V_{i,j-1,k}^{n+1}}{\delta Y} + \frac{W_{i,j,k}^{n+1} - W_{i,j,k-1}^{n+1}}{\delta Z} \right] \\
&= \left[ \frac{\tilde{U}_{i,j,k}^{n+1} - \tilde{U}_{i-1,j,k}^{n+1}}{\delta X} + \frac{\tilde{V}_{i,j,k}^{n+1} - \tilde{V}_{i,j-1,k}^{n+1}}{\delta Y} + \frac{\tilde{W}_{i,j,k}^{n+1} - \tilde{W}_{i,j,k-1}^{n+1}}{\delta Z} \right] \\
&- \delta t \left[ \frac{P'_{i+1,j,k} - 2P'_{i,j,k} + P'_{i-1,j,k}}{\delta X^2} \right] \\
&- \delta t \left[ \frac{P'_{i,j+1,k} - 2P'_{i,j,k} + P'_{i,j-1,k}}{\delta Y^2} \right] \\
&- \delta t \left[ \frac{P'_{i,j,k+1} - 2P'_{i,j,k} + P'_{i,j,k-1}}{\delta Z^2} \right] \tag{3.40}
\end{aligned}$$

The pressure corrections in the neighboring cell are neglected. Therefore, we get the velocity corrections, 3.34 to 3.39, in the form,

$$U_{i,j,k}^{n+1} \longrightarrow \tilde{U}_{i,j,k}^{n+1} + \left( \frac{\delta t}{\delta X} \right) (P'_{i,j,k}) \tag{3.41}$$

$$U_{i-1,j,k}^{n+1} \longrightarrow \tilde{U}_{i,j,k}^{n+1} - \left( \frac{\delta t}{\delta X} \right) (P'_{i,j,k}) \tag{3.42}$$

$$V_{i,j-1,k}^{n+1} \longrightarrow \tilde{V}_{i,j,k}^{n+1} + \left( \frac{\partial t}{\partial Y} \right) (P'_{i,j,k}) \quad (3.43)$$

$$V_{i,j-1,k}^{n+1} \longrightarrow \tilde{V}_{i,j,k}^{n+1} - \left( \frac{\partial t}{\partial Y} \right) (P'_{i,j,k}) \quad (3.44)$$

$$W_{i,j,k+1}^{n+1} \longrightarrow \tilde{W}_{i,j,k}^{n+1} + \left( \frac{\partial t}{\partial Z} \right) (P'_{i,j,k}) \quad (3.45)$$

$$W_{i,j,k+1}^{n+1} \longrightarrow \tilde{W}_{i,j,k}^{n+1} - \left( \frac{\partial t}{\partial Z} \right) (P'_{i,j,k}) \quad (3.46)$$

The continuity equation takes the following form after neglecting the pressure corrections in the neighboring cells,

$$\begin{aligned} & \left[ \frac{U_{i,j,k}^{n+1} - U_{i-1,j,k}^{n+1}}{\delta X} + \frac{V_{i,j,k}^{n+1} - V_{i,j-1,k}^{n+1}}{\delta Y} + \frac{W_{i,j,k}^{n+1} - W_{i,j,k-1}^{n+1}}{\delta Z} \right] \\ &= \left[ \frac{\tilde{U}_{i,j,k}^{n+1} - \tilde{U}_{i-1,j,k}^{n+1}}{\delta X} + \frac{\tilde{V}_{i,j,k}^{n+1} - \tilde{V}_{i,j-1,k}^{n+1}}{\delta Y} + \frac{\tilde{W}_{i,j,k}^{n+1} - \tilde{W}_{i,j,k-1}^{n+1}}{\delta Z} \right] \\ &+ 2 \left( \frac{\partial t}{\delta X^2} \right) (P'_{i,j,k}) + 2 \left( \frac{\partial t}{\delta Y^2} \right) (P'_{i,j,k}) + 2 \left( \frac{\partial t}{\delta Z^2} \right) (P'_{i,j,k}) \end{aligned} \quad (3.47)$$

or,

$$0 = \Delta_{i,j,k} + P'_{i,j,k} \left[ 2 \partial t \left[ \frac{1}{\delta X^2} + \frac{1}{\delta Y^2} + \frac{1}{\delta Z^2} \right] \right] \quad (3.48)$$

or

$$P'_{i,j,k} = \omega_0 (\Delta_{i,j,k}) / \left[ 2 \partial t \left[ \frac{1}{\delta X^2} + \frac{1}{\delta Y^2} + \frac{1}{\delta Z^2} \right] \right] \quad (3.49)$$

Where  $\omega_0$  is an over relaxation factor which is introduced to accelerate the pressure correction process. Usually a value of 1.7 is used. After calculating  $\partial P'_{i,j,k}$ , velocities in each cell are corrected according to the equation set and pressure in each cell is adjusted as

$$P_{i,j,k}^{n+1} \longrightarrow P_{i,j,k}^n + P'_{i,j,k} \quad (3.50)$$

This process is continued until the velocity divergence in each cell vanishes. If the velocity boundary conditions are correct and a divergence free converged velocity field is obtained, eventually correct pressure will be evolved in all the cells including the cells on the boundary. This feature of modified MAC method has been discussed in more details by Peyret and Taylor (1983). However, it was also shown by Brandt, Dendy and Ruppel (1980) that the aforesaid pressure velocity iteration procedure is equivalent to the solution of Poisons equation for pressure.

### 3.7 Solution of the Energy Equation

After evaluating the steady state velocities, the energy equation is solved by Successive Over-Relaxation technique to determine the temperature field. The procedure adopted for this is presented in this section. The steady state energy equation, neglecting the dissipation term, may be written in the following conservative form as

$$\frac{\partial U\theta}{\partial X} + \frac{\partial V\theta}{\partial Y} + \frac{\partial W\theta}{\partial Z} = \frac{\nabla^2 \theta}{Pe} \quad (3.51)$$

Equation [ 3.51 ] may be written as

$$\nabla^2 \theta = Pe[CONVT]_{i,j,k}^m \quad (3.52)$$

where,  $[CONVT]_{i,j,k}$  is the discretized convective terms on the left hand side of equation (3.39) and  $m$  stands the iterative counter. To start with we can assume any guess value of  $\theta$  throughout the flow field. The velocities  $U, V$  and  $W$  are known from the solution of momentum equation and hence equation (3.39) is now a linear equation. Using the guess values of  $\theta$  and known values of  $U, V, W$  the left hand side of equation (3.52) is evaluated. A weighted average scheme is adopted for discretisation of the convective terms. After discretizing and evaluating the right hand side of equation (3.52) we obtain a Poisson equation for temperature with a source term on the right hand side. Now, we can follow a SOR technique for solving equation (3.52). Consider a discretized equation as

$$\frac{\theta_{i+1,j,k} - 2\theta_{i,j,k} + \theta_{i-1,j,k}}{(\delta X)^2} + \frac{\theta_{i,j+1,k} - 2\theta_{i,j,k} + \theta_{i,j-1,k}}{(\delta Y)^2} + \frac{\theta_{i,j,k+1} - 2\theta_{i,j,k} + \theta_{i,j,k-1}}{(\delta Z)^2} = S^{*m} \quad (3.53)$$

where  $S^{*m} \equiv Pe[CONVT]_{i,j,k}^m$

The equation is solved by the SOR method with right hand side being updated after each iterative sweep.

### 3.8 Stability Criteria

For a given mesh the choice of time step is determined through stability analysis which has to take care of two conditions. First, fluid should not be allowed to cross more than one cell in one time step. The restriction is derived from the Courant Friedrich-Lewy (CFL) condition given by

$$\delta t_1 < \min\left(\frac{\delta X}{|U|}, \frac{\delta Y}{|V|}, \frac{\delta Z}{|W|}\right) \quad (3.54)$$

Where the minimum is with respect to every cell in the domain. Typically  $\delta t$  is chosen equal to one- third to two third of the minimum cell transient time. Second, when a non -

zero value of kinematic viscosity is used, momentum must not diffuse more than approximately one cell in one time step. A linear stability analysis shows that the restriction on grid Fourier number will yield

$$\delta t_2 < \frac{1}{2} / \left( \frac{1}{\delta X^2} + \frac{1}{\delta Y^2} + \frac{1}{\delta Z^2} \right) \text{Re} \quad (3.55)$$

Finally, the minimum of the two time steps is chosen for the computation.

The term  $\alpha$  in the discretization of convective terms of the equations, which is a weighing factor which gives the desired amount of upstream (donor cell) differencing and  $\alpha=1$  gives full upstream or donor cell form, which is stable provided the fluid is not permitted to cross more than one cell in one time-step. In general,  $\alpha$  should be chosen slightly larger than the maximum value of

$$\left| \frac{U \partial t}{\delta X} \right| \text{ or } \left| \frac{V \partial t}{\delta Y} \right| \text{ or } \left| \frac{W \partial t}{\delta Z} \right| \quad (3.56)$$

Occurring in the entire domain. In other words

$$1 > \alpha > \max \left[ \left| \frac{U \partial t}{\delta X} \right|, \left| \frac{V \partial t}{\delta Y} \right|, \left| \frac{W \partial t}{\delta Z} \right| \right] \quad (3.57)$$

The given flow chart (Fig. 3.5 ) shows the overall structure of the Transient flow MAC algorithm and its variants.

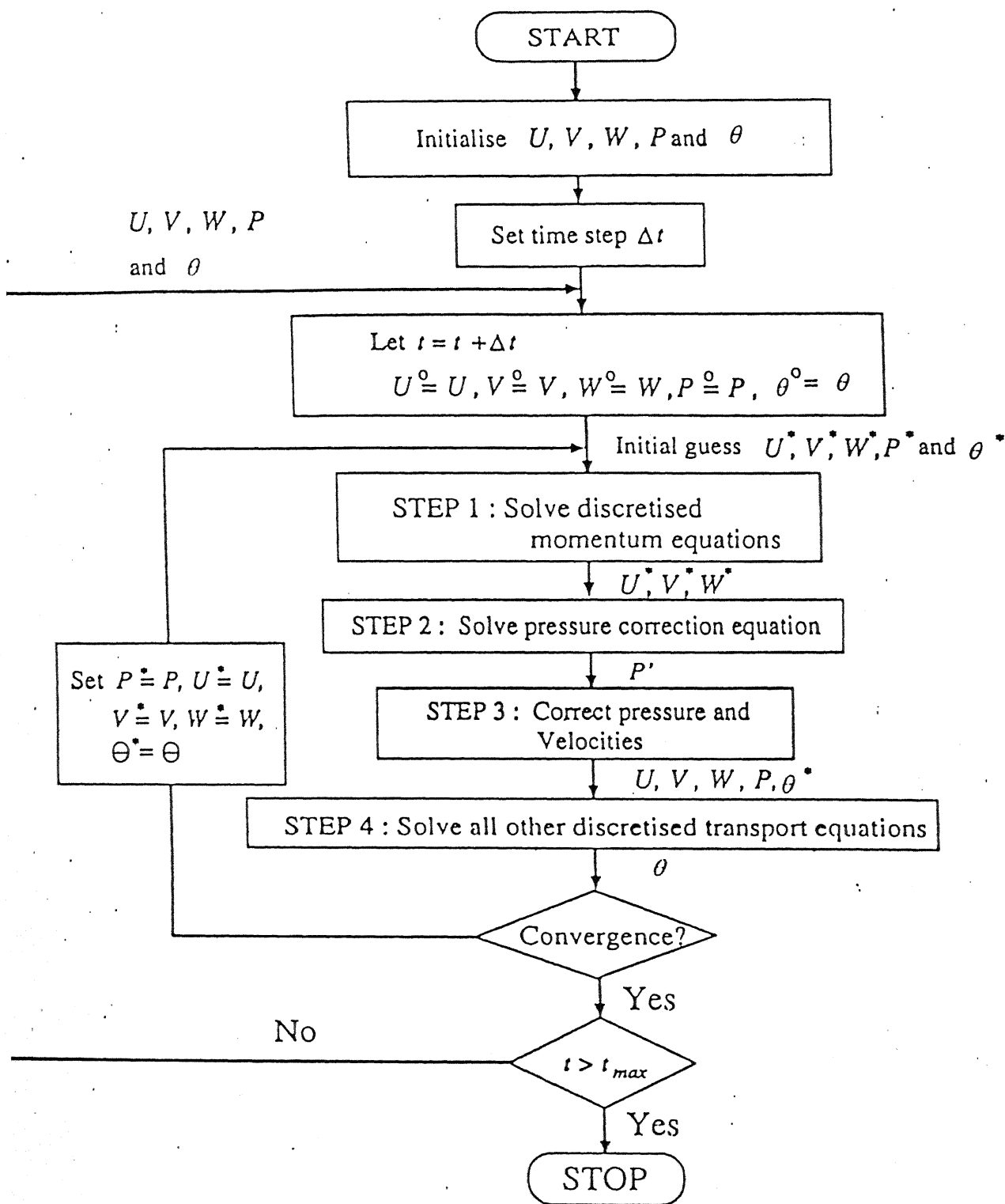


Figure 3.5 Flow Chart : Transient flow MAC algorithm and its variants

## CHAPTER 4

### RESULTS AND DISCUSSIONS

Ribs are usually set in a row in the streamwise direction. This continuous form of rib attachment creates a roughened wall and generates oscillatory motion. In this chapter the oscillatory flow behind the surface mounted rib is explained with the help of mean streamwise and transverse velocity profiles, streamwise and transverse rms velocity profiles, power spectrum, shear stress profiles, velocity contours and vorticity contours. The effect on heat transfer is explained with the help of Nusselt number distribution. The effect of Reynolds number on the flow characteristics is also explained. The presentation of this chapter starts with the validation of the code through grid independence study and reestablishing the results from available literature using the code.

#### 4.1 Validation Study

The grid independence study was performed by comparing the results obtained using two different grid-meshes, such as 70X42X20 and 82X46X26 in X,Y and Z directions respectively. Fig. 4.1 (a) & (b) show the time averaged mean streamwise ( $\bar{u}$ ) velocity profile at  $x=4h$  and  $x=18h$  locations respectively obtained using two different grid - meshes. The nature of variation is very much similar for two different grid-meshes considered here. The maximum discrepancy between the two profiles is about 5%. This confirms the grid independence of the result presented in this work. For all the subsequent cases 70X42X20 grid-mesh was used.

GRID INDEPENDENCE STUDY ( $x = 4h$ )  $Re = 2500$

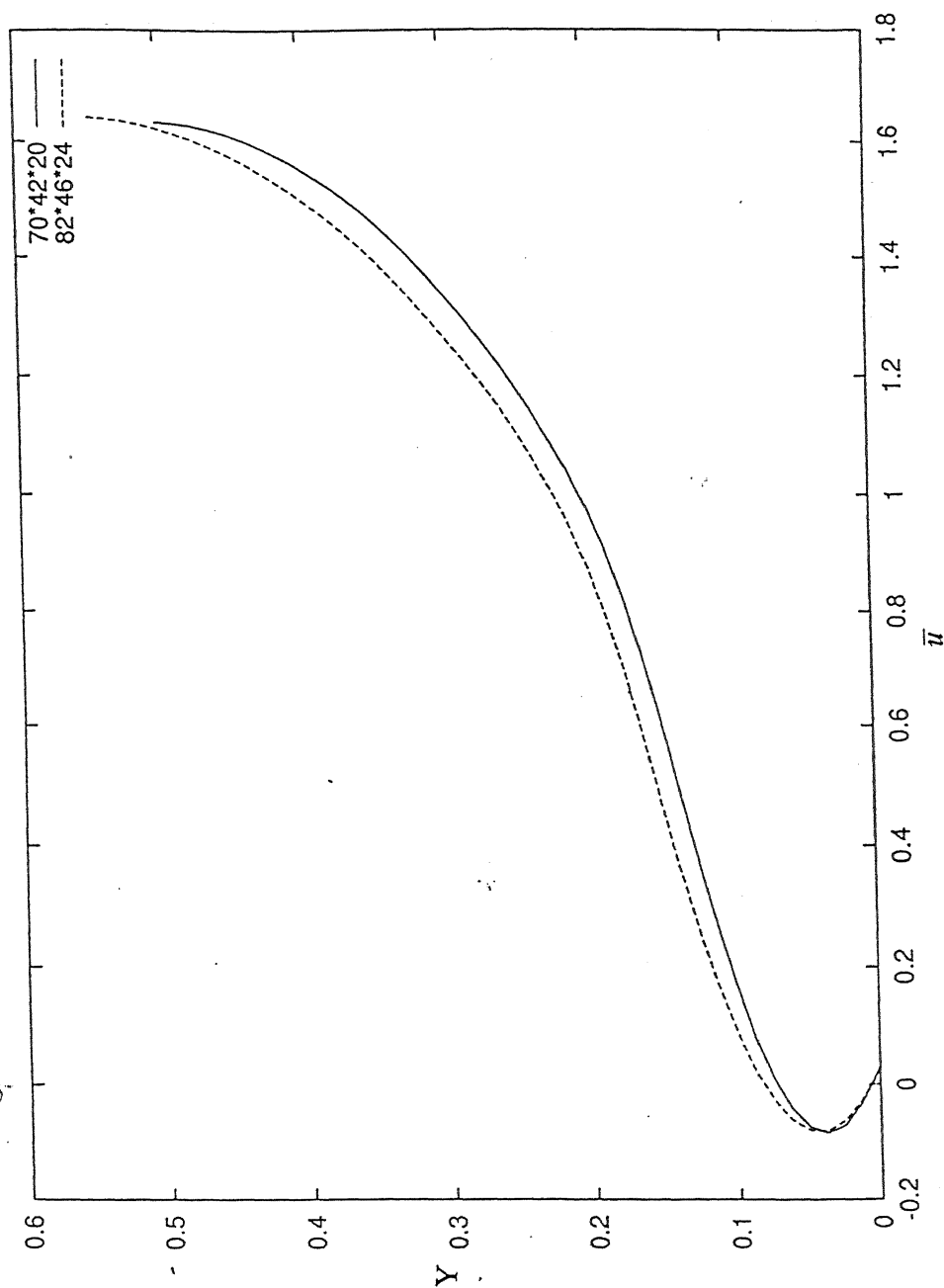


Figure 4.1 (a) Time averaged mean streamwise velocity profile at  $x=4h$



GRID INDEPENDENCE STUDY ( $x = 18h$ )  $Re = 2500$

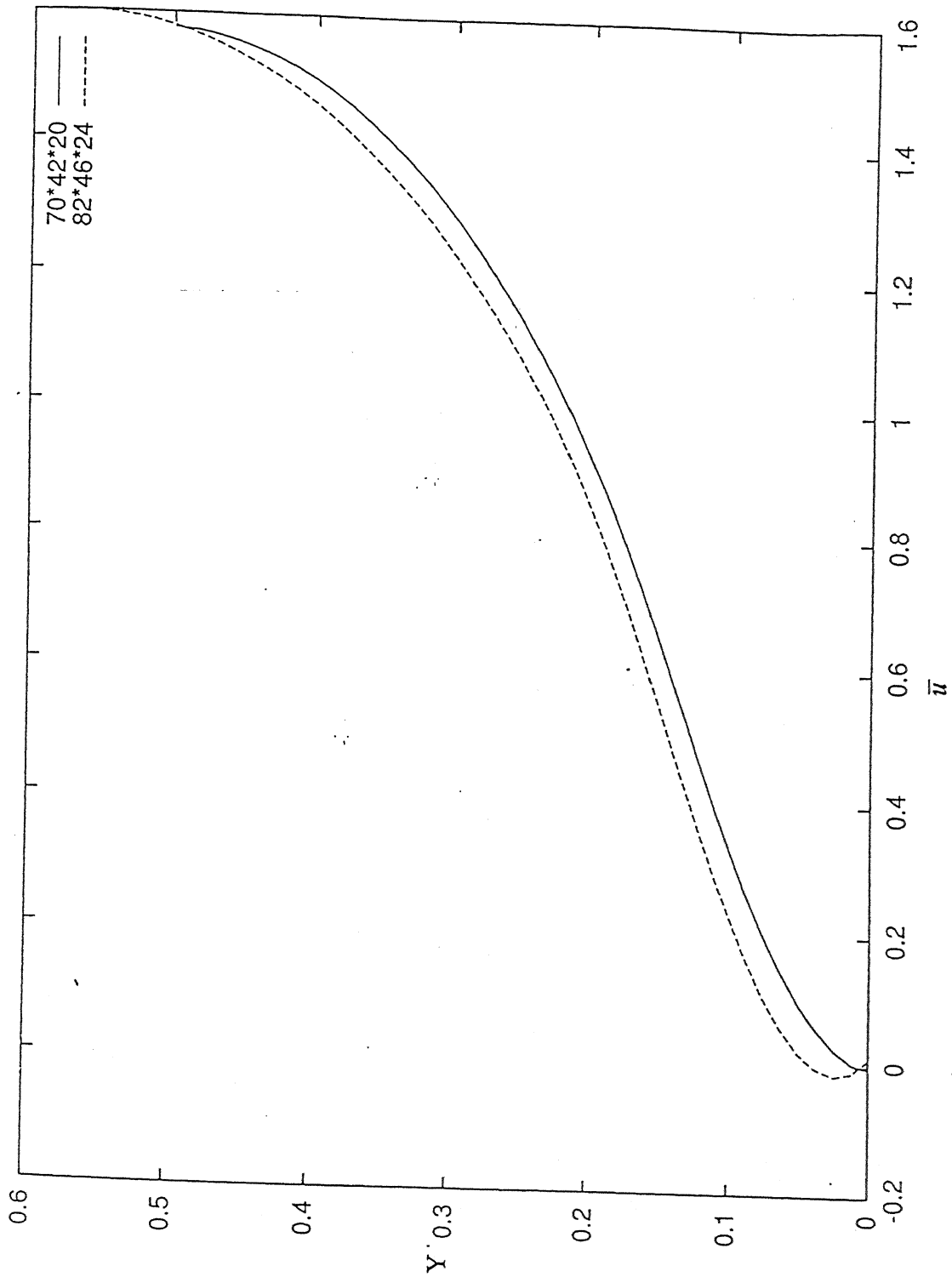


Figure 4.1 (b) Time averaged mean streamwise velocity profile at  $x=18h$

Next, the comparison is made for the plane channel case between the results obtained from the current numerical calculation and the analytical and experimental results available in the literature at a Reynolds number of 125, based on the channel height. Figure 4.2 shows the streamwise variation of  $f_{XRe}$  for the hydrodynamically developed flow in a channel. The  $f_{XRe}$  is not only a constant in the streamwise direction but also equal to the analytical value of 24.

Figure 4.3 shows the variation of  $f_{XRe}$  in the streamwise direction of a plane channel where, the flow is hydrodynamically developing, i.e. the flow has a uniform velocity profile at the entrance of the channel. As expected, the  $f_{XRe}$  value decreases in the streamwise direction to the fully developed value of 24. The  $f_{XRe}$  value is higher in the developing region due to the presence of higher value of the velocity gradient. Thus, the results obtained using the current code satisfies the flow physics. To further verify the quantitative result,  $f_{XRe}$  value obtained here is compared with what was obtained by Shah and London (1978) as :

$$f_{app} Re = \frac{3.44}{(x^+)^{1/2}} + \frac{24 + 0.674[(4x^+) - 3.44](x^+)}{1 + 0.000029(x^+)^{-2}}$$

where, axial coordinate for the hydrodynamic entrance region,  $x^+ = x/D_h Re$

$D_h$  = hydraulic diameter of the flow passages,  $4r_h$

It may be verified from Fig.4.3 that the  $f_{XRe}$  results obtained from the numerical calculation are in good agreement with that of Shah and London, with the exceptions at very close to the entrance of the channel. This can be attributed to the comparatively coarse grid used in the current investigations. As the velocity gradient is highest at the entrance to the channel, finer grid is required to resolve the steep gradients. This was verified by using coarser grid than the one used in the current work and the variation between the numerical and analytical results was found to be more in the entrance region. Due to the computational constraint, the results were not obtained for the finer grid-meshes.

CODE VALIDATION  $Re(H) = 125$

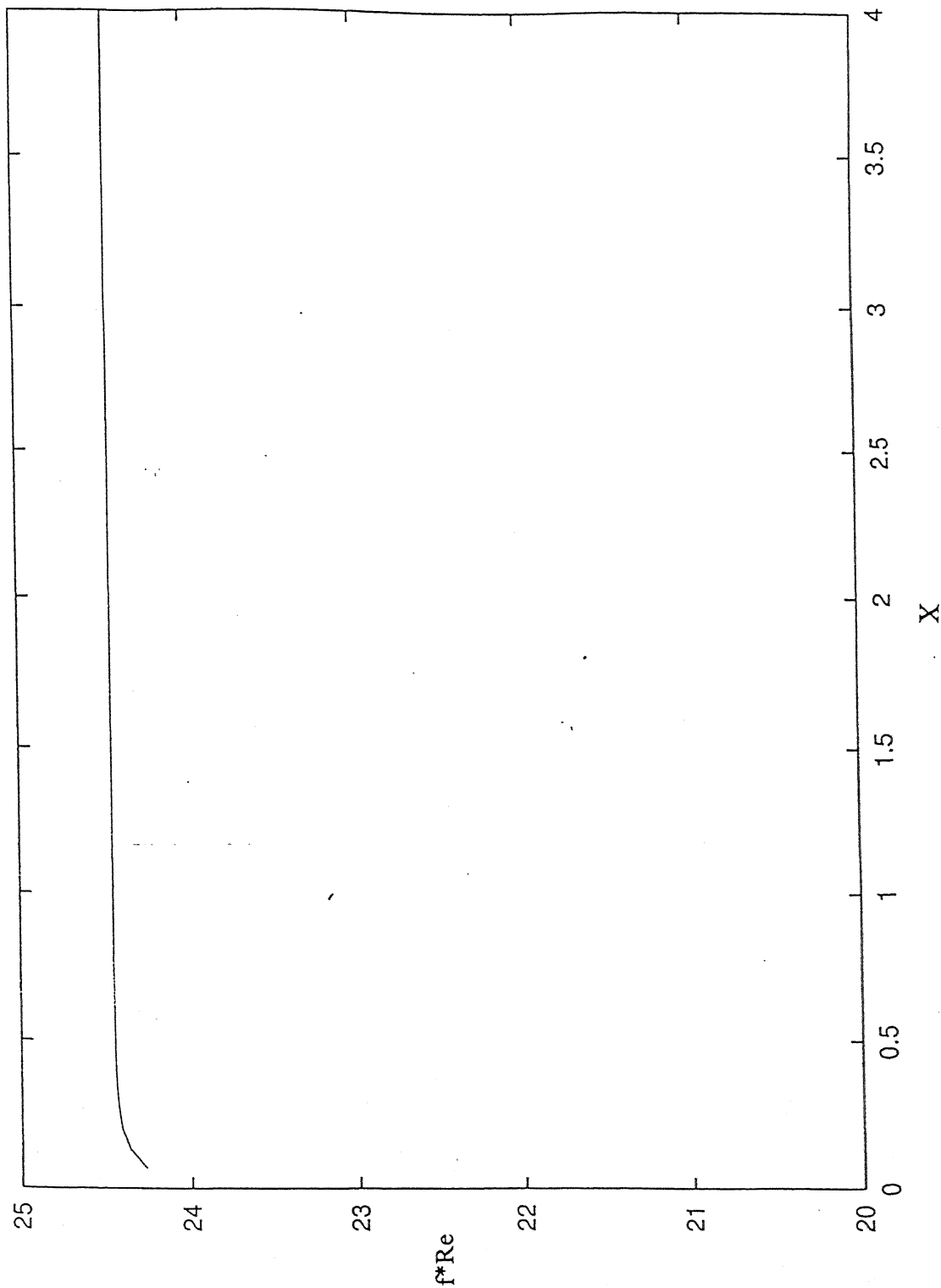
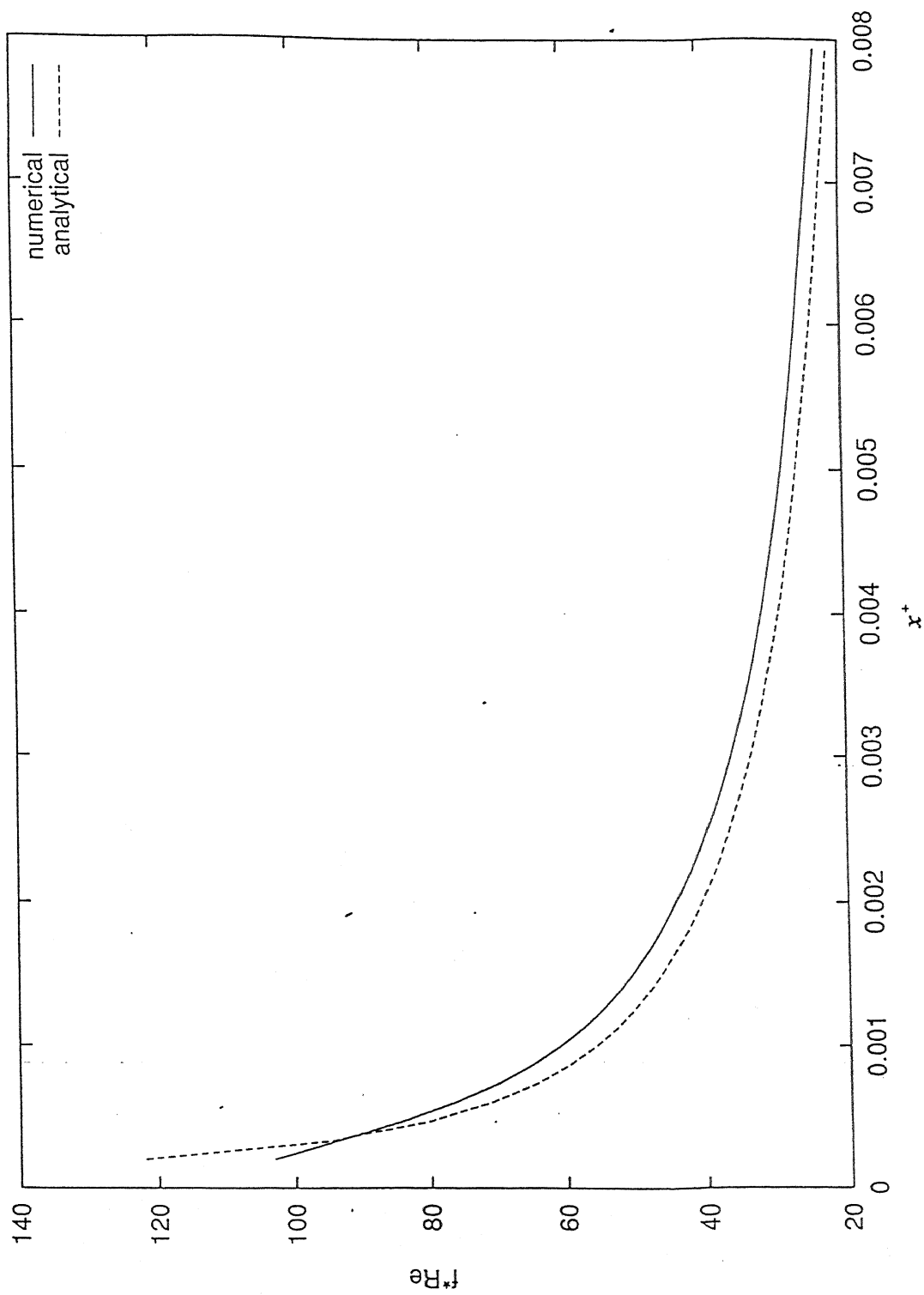


Figure 4.2 Variation of  $f^*Re$  along the channel length



The verification of heat transfer calculation was done by comparing the Nusselt number distribution in the streamwise direction for a hydrodynamically developed flow and thermally developing flow ( Figure 4.4). It is observed that the Nusselt number decreases in the streamwise direction to a constant value corresponding to the thermally developed case. The thermally developed Nusselt number obtained here is about 7.9570 which is very close to the value predicted from the analytical solution (7.671981). The detailed quantitative assessment is made by comparing with the results of Shah and London (1978).

$$Nu_{x,T} = \begin{cases} 1.233(x^*)^{-1/3} + 0.4 & \text{for } x^* \leq 0.001 \\ 7.541 + 6.874(10^3 x^*)^{-0.488} e^{-245 x^*} & \text{for } x^* > 0.001 \end{cases}$$

where axial co-ordinate for the thermal entrance region,  $x^* = x/D_h \text{ Re}$  and  $D_h$  is the hydraulic diameter of the actual duct,  $4r_h$ .

The Nusselt number value obtained from the current numerical simulation is within 0.5 % of the value obtained using the above expression of Shah and London with the exception of the entrance region of the channel. The discrepancy in the entrance region can be attributed to the improper grid size used therein.

## 4.2 Mean Velocity Results :

The mean streamwise velocity profile for  $\text{Re} = 2500$  based on the channel height, at various  $X$  locations is presented in Figure 4.5. The recirculating region presented behind the rib is evident from the negative velocity observed in the region corresponding to smaller  $x/h$ . The nature of variation of the time averaged streamwise mean  $u$ -velocity is similar to that of Tropea and Gackstatter (1985). At the far field location ( $x/h = 34$  &  $44$ ), as shown in Figure 4.5(d), the velocity profile is similar indicating that the fully developed flow is established downstream of the rib.

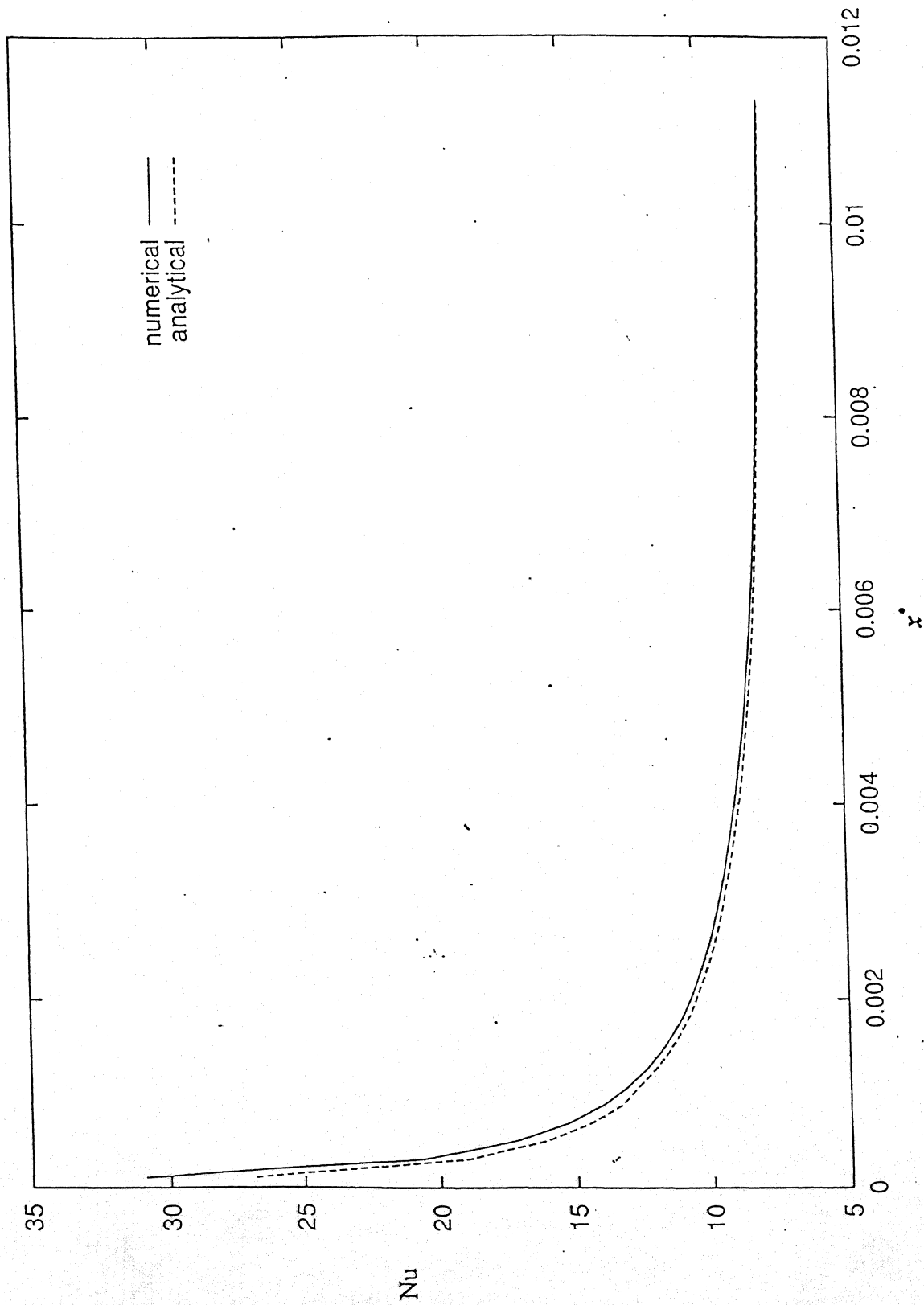


Figure 4.4 Nusselt number variation along the thermal entrance for hydrodynamically developed flow

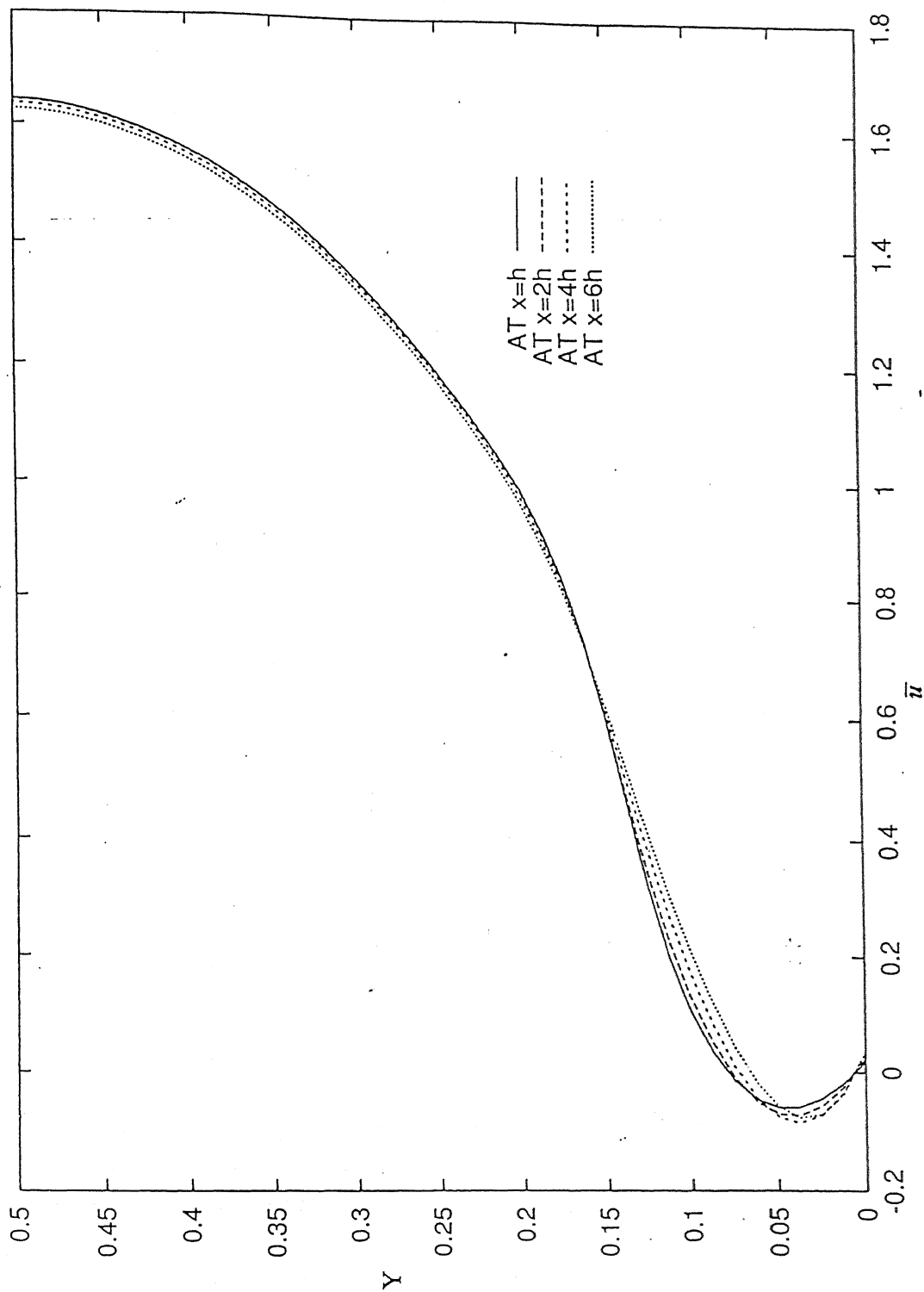


Figure 4.5 (a) Variation of time averaged mean streamwise velocity at different locations in the downstream

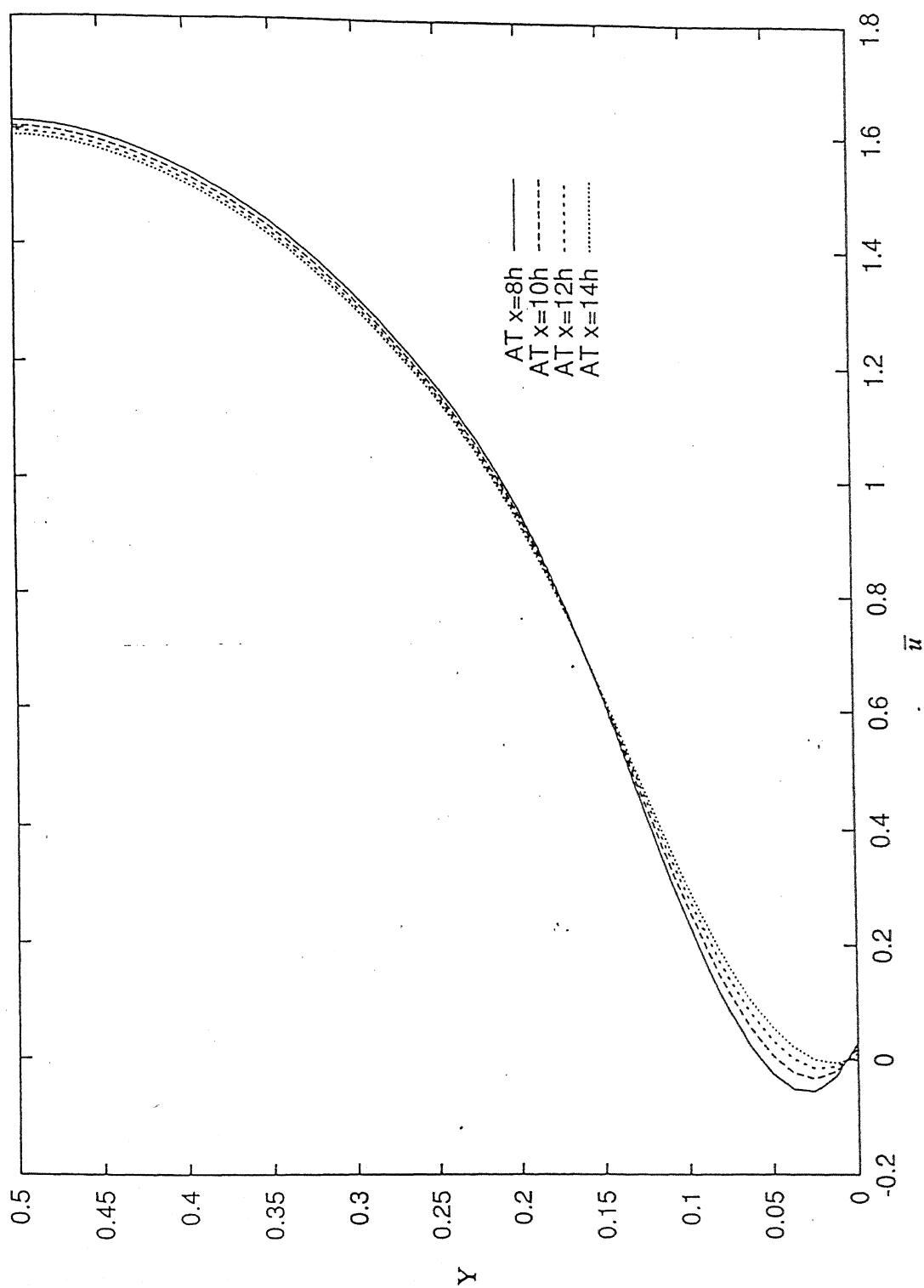


Figure 4.5 (b) Variation of time averaged mean streamwise velocity at different locations in the downstream



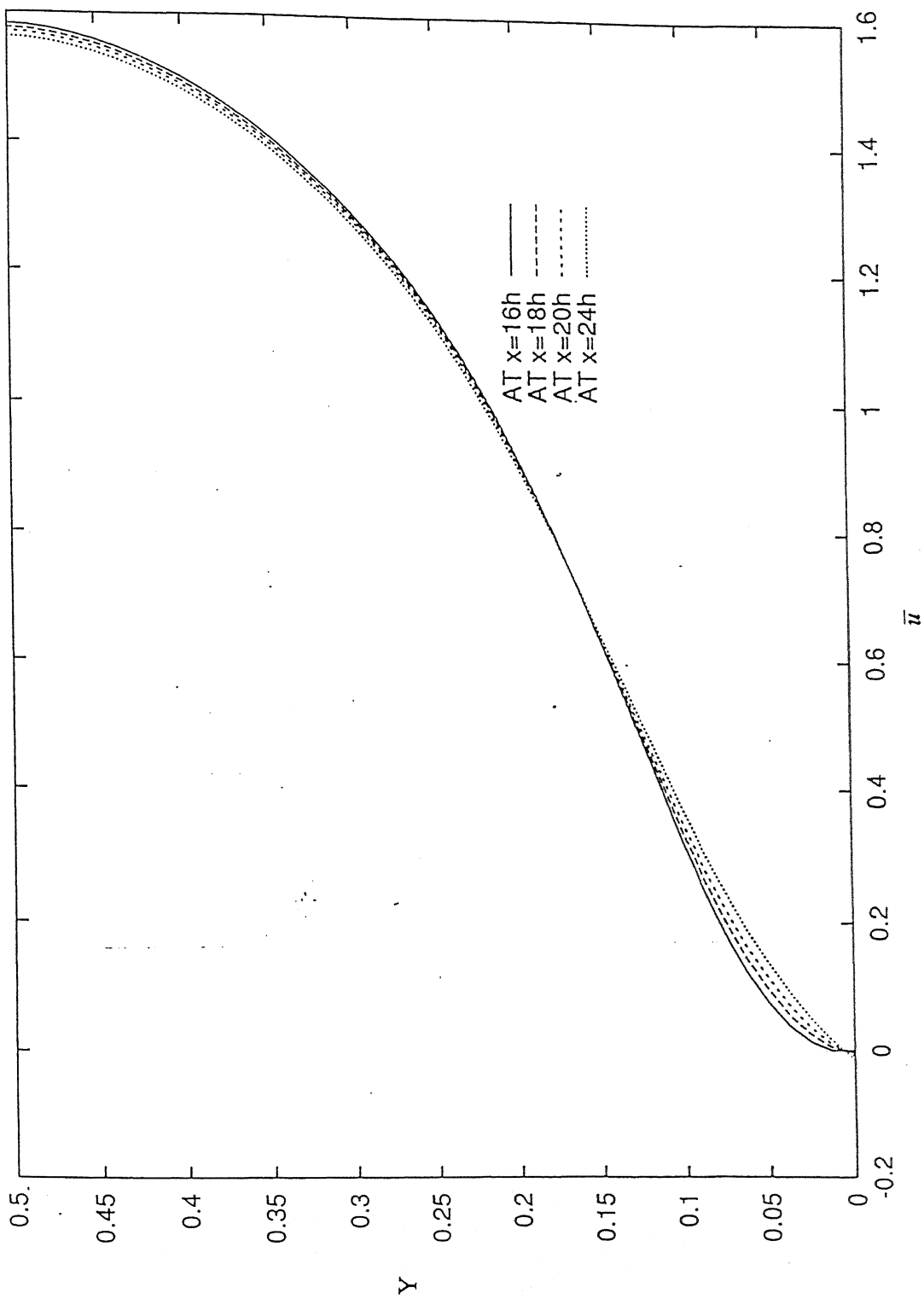


Figure 4.5 (c) Variation of time averaged mean streamwise velocity at different locations in the downstream

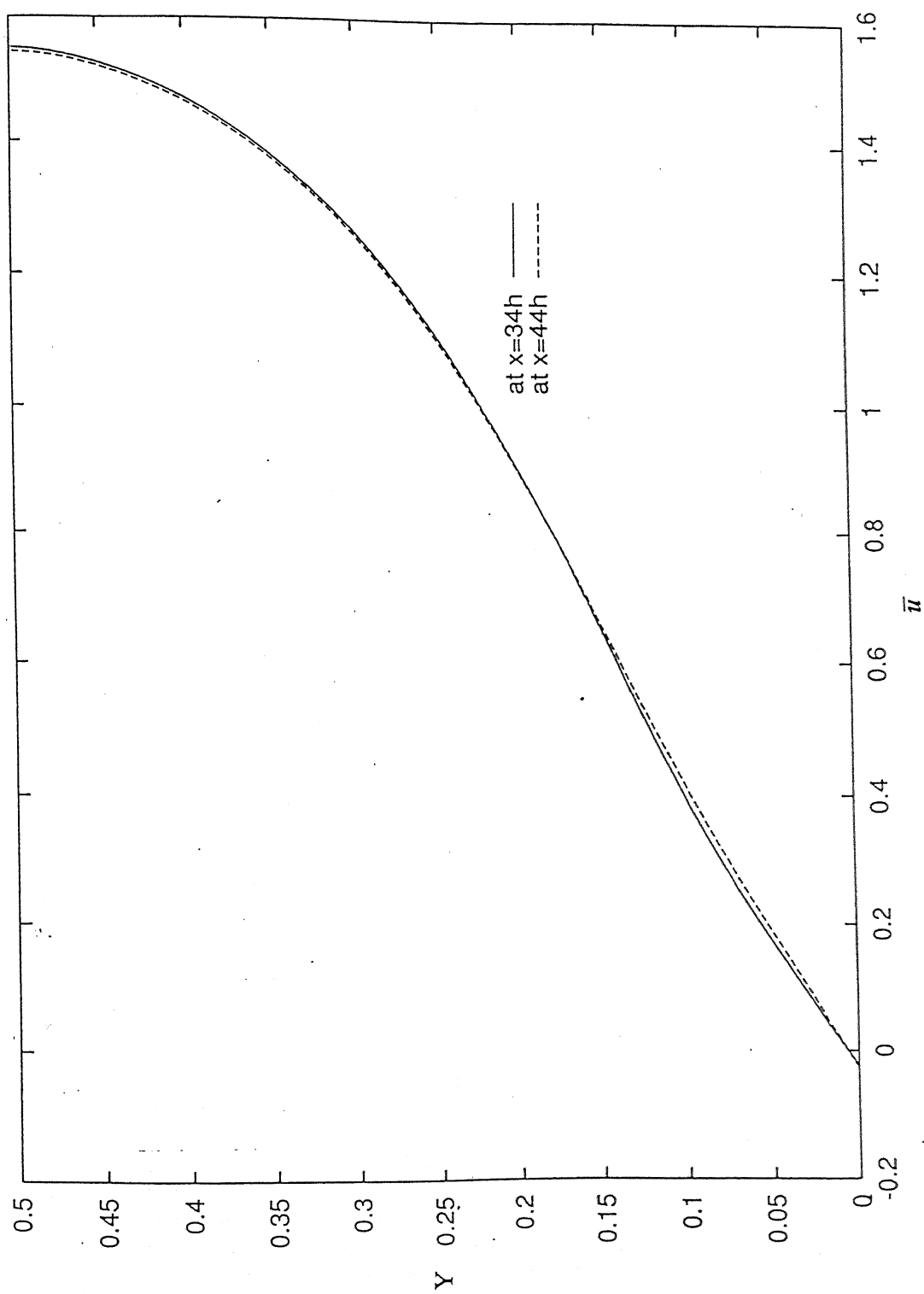


Figure 4.5 (d) Variation of time averaged mean streamwise velocity at different locations in the downstream

The reattachment length is the distance at which the intermittency in the velocity profile is 50 %, i.e. the velocity is equally probable in the forward and backward direction. At the reattachment length, the mean streamwise velocity should be equal to zero. From Fig. 4.6, the reattachment location is observed to be about  $x/h = 16$ . Tropea and Gackstatter have shown the variation of reattachment length with Reynolds number. At the Reynolds number of 2500 the reattachment length is equal to  $15h$ . The numerical results obtained here compare well with the experimental results of Tropea and Gackstatter.

The time averaged transverse velocity ( $\bar{v}$ ) profiles at different streamwise ( $X$ ) locations are presented in Figure 4.6. In the region of lower  $x/h$  values the  $v$ -velocity increases from the bottom of the channel and then decreases. The  $v$ -velocity is positive close to the bottom surface. This is because, the streamlines get deflected upward due to the presence of the obstacle. The upward deflection of the streamlines is indicated by the positive  $v$ -velocity. In the region of higher  $x/h$  value, the  $\bar{v}$  velocity is always negative. This is an indication of the downstream deflection of the streamlines behind the rib, i.e. the flow tends to reattach and then the flow moves in the downward direction. The  $v$ -velocity profile is shown in Fig 4.6 is similar to the numerical and experimental results obtained by Acharya et al (1994) for a square rib mounted on the surface of a channel.

### 4.3 Reynolds Stresses Profile:

In this section, the normal stress and shear stress components of the Reynolds stress contribution are discussed. In Fig. 4.7 the  $u$ -velocity fluctuations is presented. The RMS velocity fluctuation in general increases away from the bottom surface to a maximum value and then decreases to a small value at the center of the channel. The higher RMS value corresponds to the core of the reattaching shear layer. The maximum value of turbulence fluctuation at the core

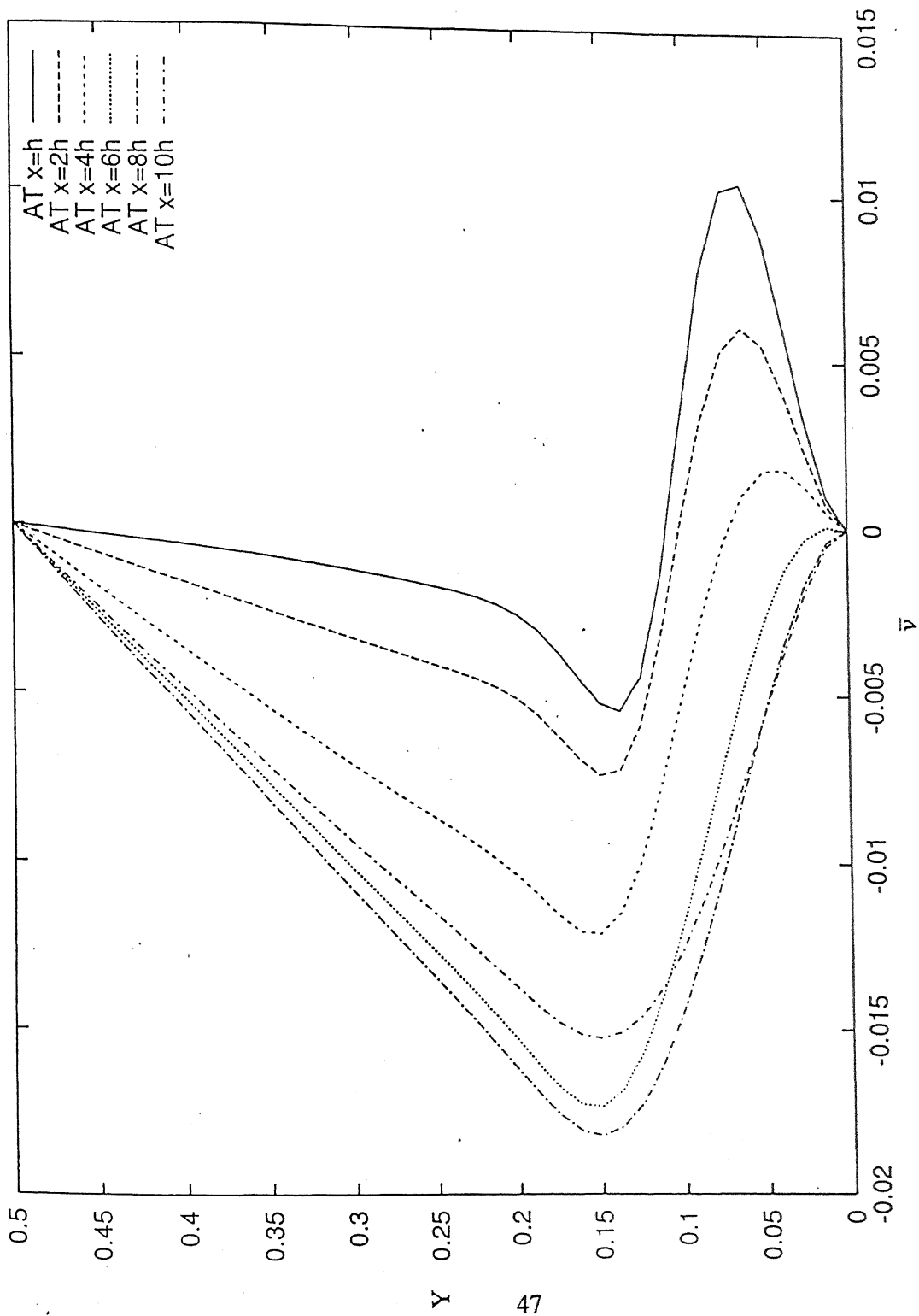


Figure 4.6 (a) Variation of time averaged mean transverse velocity at different locations in the downstream

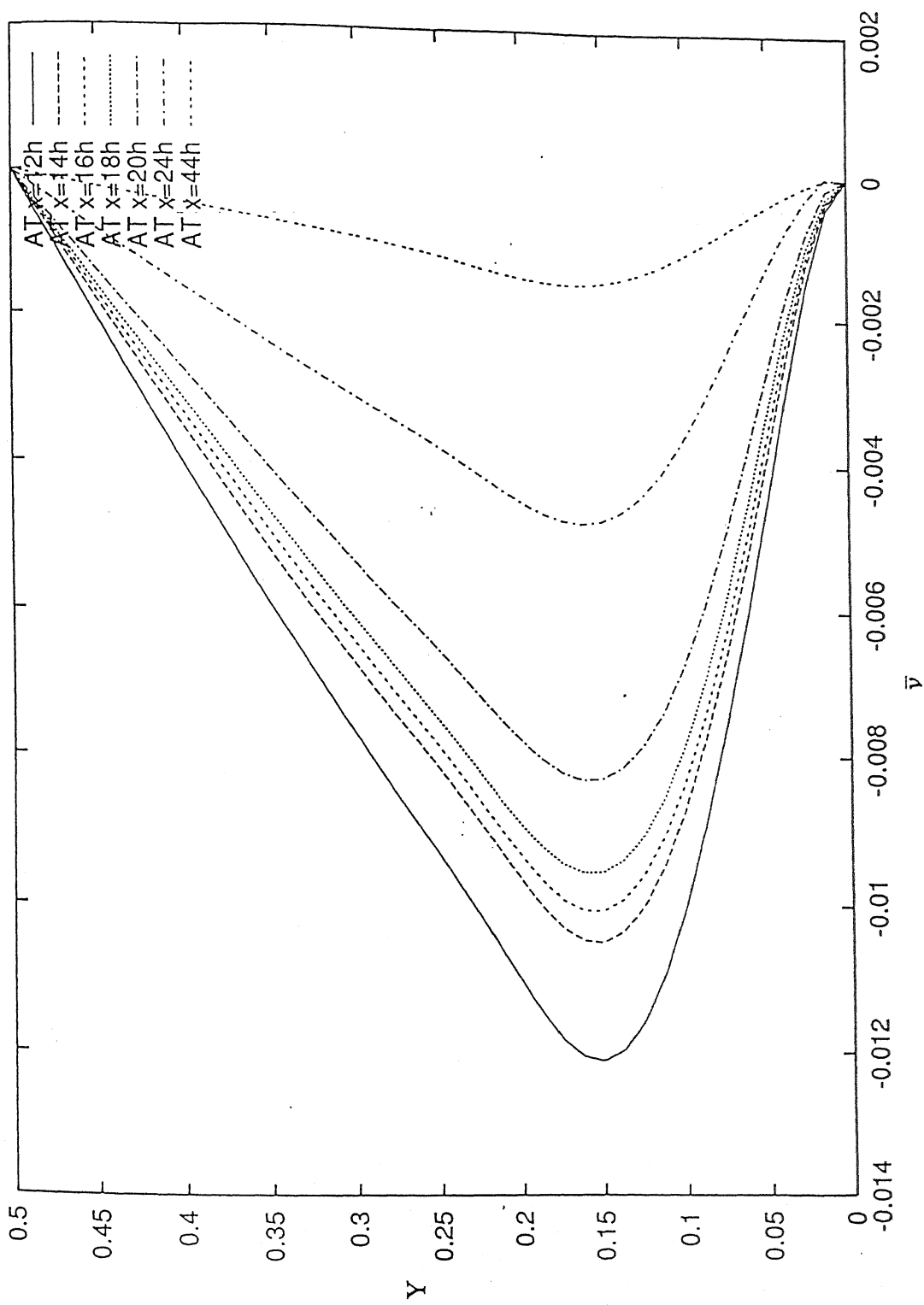


Figure 4.6 (b) Variation of time averaged mean transverse velocity at different locations in the downstream

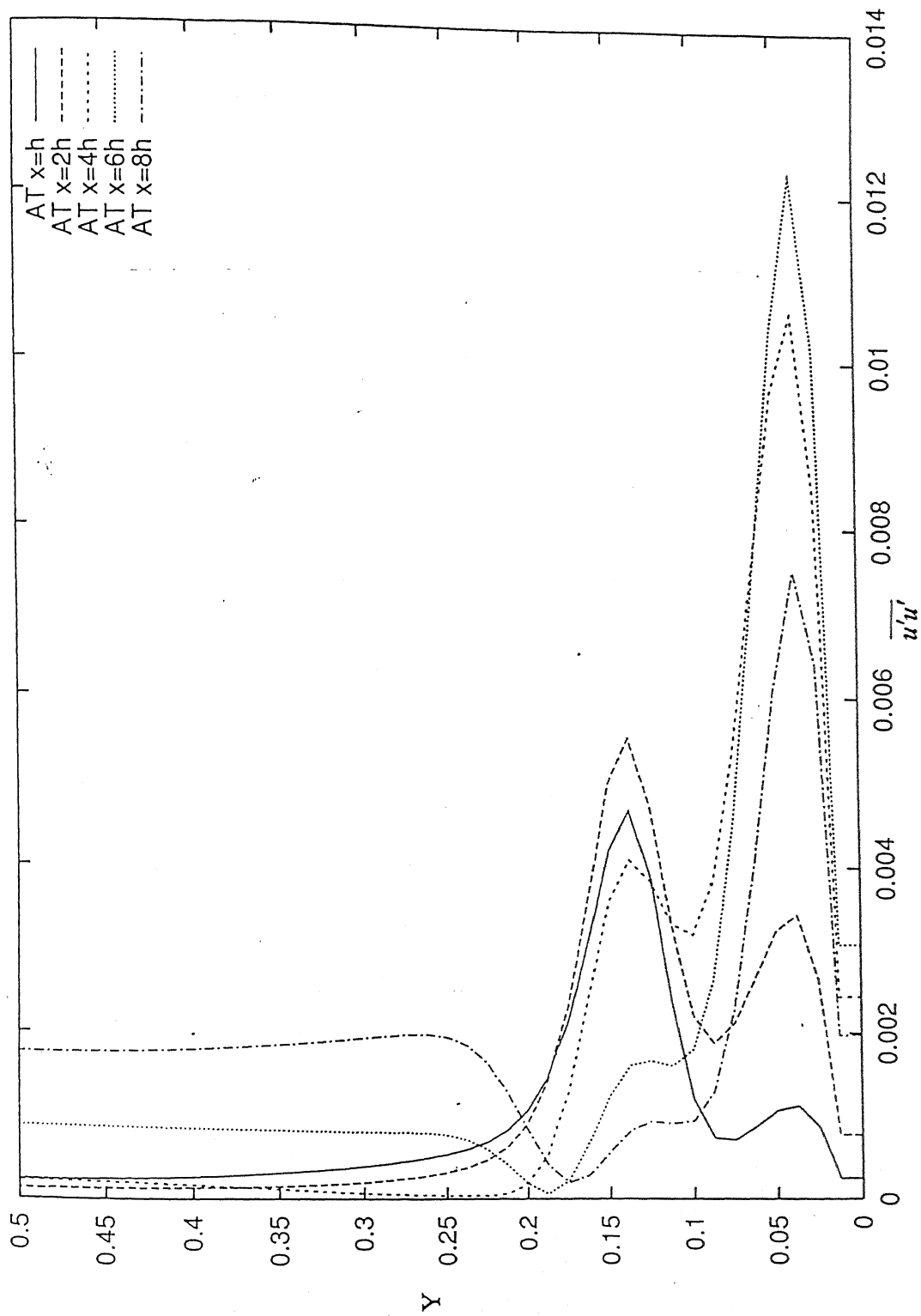


Figure 4.7 (a) Variation of time averaged streamwise normal stress at different locations in the downstream

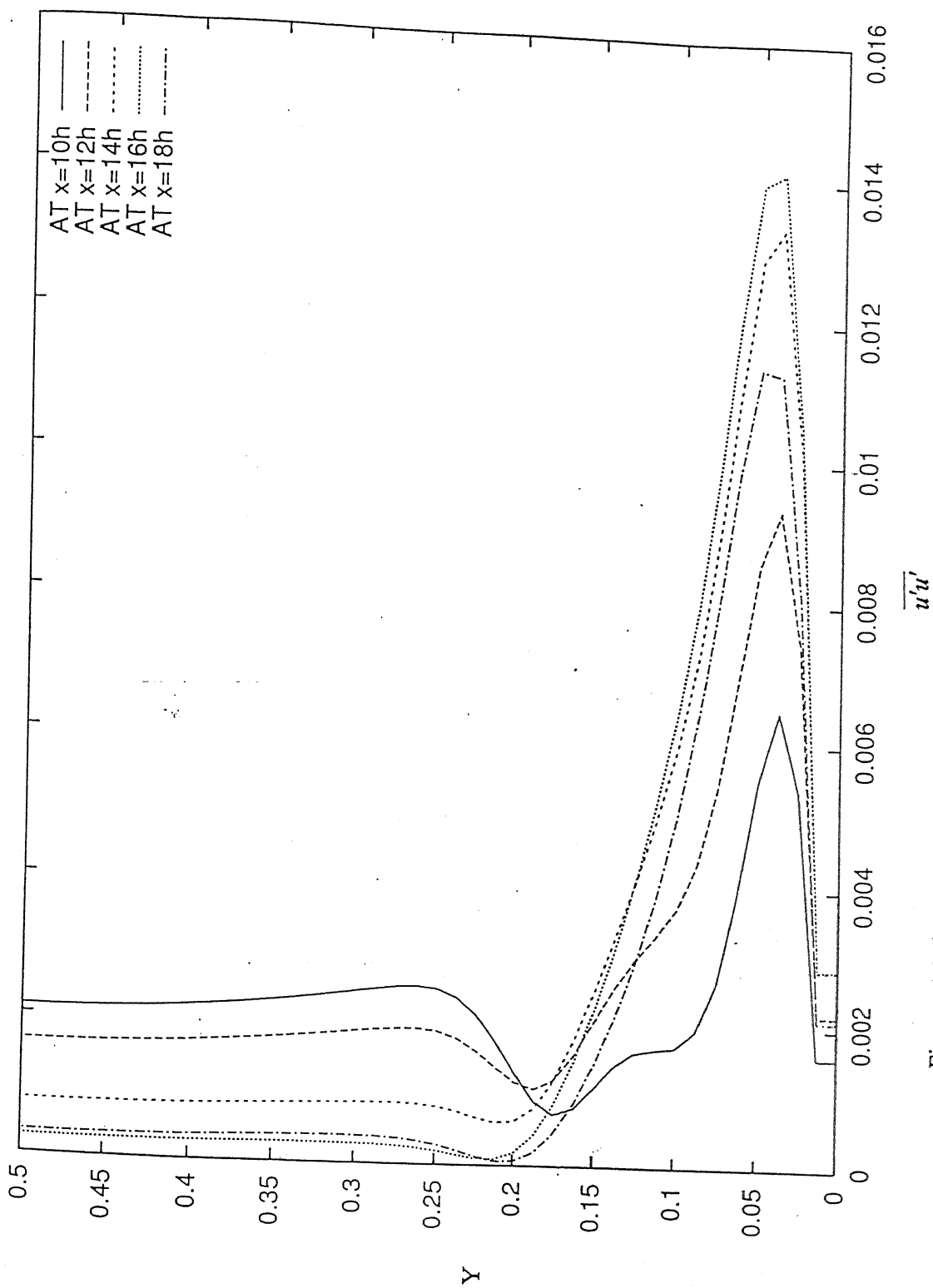


Figure 4.7 (b) Variation of time averaged streamwise normal stress at different locations in the downstream

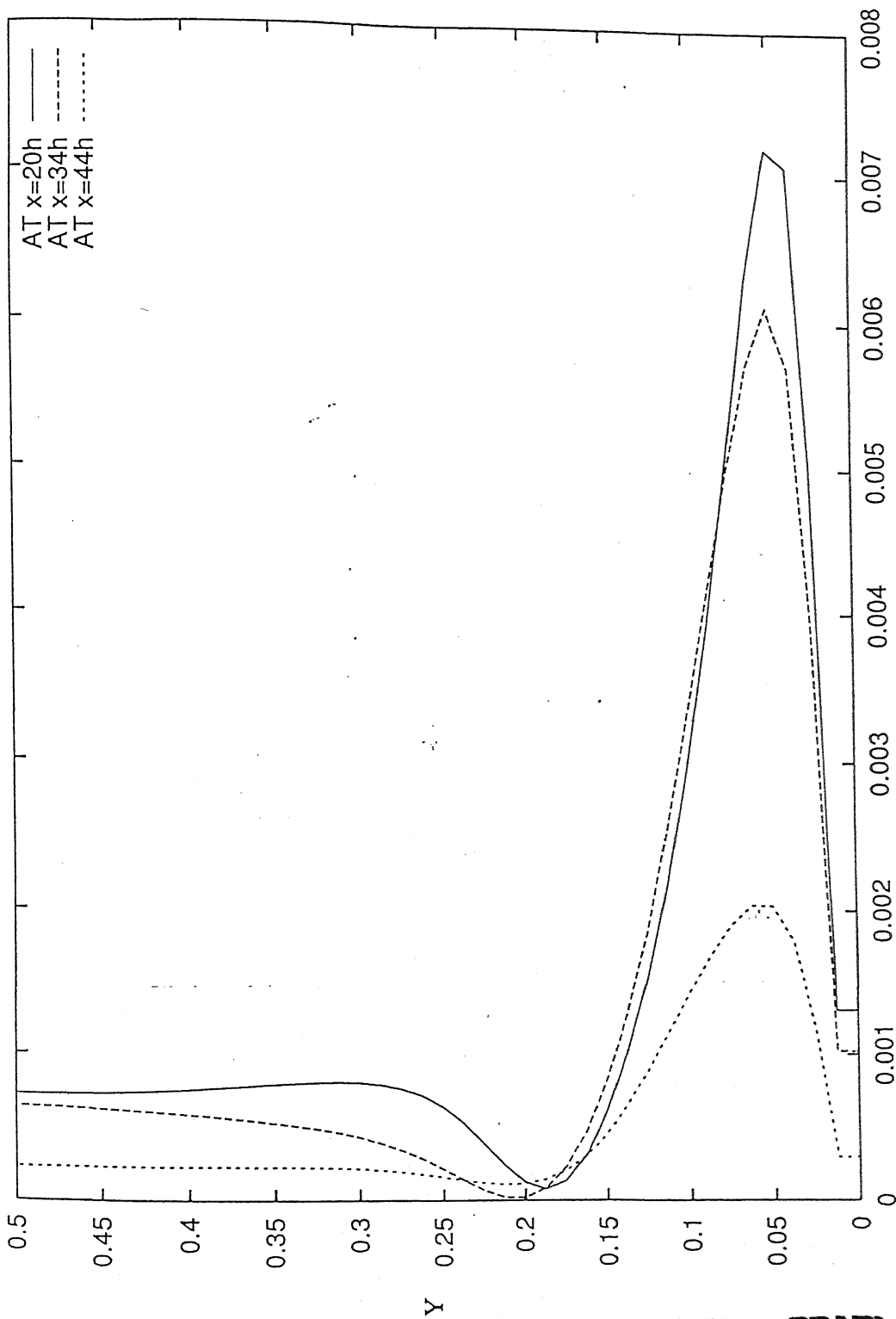


Figure 4.7 (c) Variation of time averaged streamwise normal stress at different locations in the downstream



of the shear layer is due to the higher value of the velocity gradient. In the center of the channel, the  $u_{rms}$  value is lower indicating smaller production rate of turbulence because of the smaller velocity gradient.

Comparing the  $u_{rms}$  fluctuation profile with that of Acharya et. al. (1994), it may be observed that both the results compare well at the far field region. But, at the near field region, present numerical result predicts two peaks which is not observed in the results of Acharya et. al. (1994). It should be noted that, for the cylinder in the free stream case, two peaks are observed signifying the vortex shedding from the bottom and the top surface of the cylinder. The presence of two peaked RMS fluctuation indicates the presence of two different types of vortex shedding. It is speculated that this may be due to the fact that some of the vortices are deflected in the downward direction while some get convected away in the streamwise direction such that each corresponds to the two different peaks in the RMS fluctuation. The  $v$  – velocity fluctuation in the streamwise direction is shown in Fig. 4.8. The general nature of  $v$  – velocity fluctuation is similar to what has been seen by Acharya et. al. (1994). It should be noted that the  $Y$ - location of maximum  $v$  – fluctuation is higher than that of the  $u$  – fluctuation . Similar observation was made by Panigrahi (1997). This variation can be justified from the fact that the effect of wall is more pronounced for the  $v$  – velocity than the  $u$  – velocity because of the continuity equation.

The shear stress contribution of the Reynolds stress is presented in Fig. 4.9. The shear stress is observed to increase away from the bottom surface and then decreases. The shear stress distribution is broader than the normal stress variation. This may be attributed to the fact that the  $u$  – fluctuation and  $v$  – fluctuation take place at different transverse ( $Y$ ) location.

#### 4.4 Average Pressure Distribution :

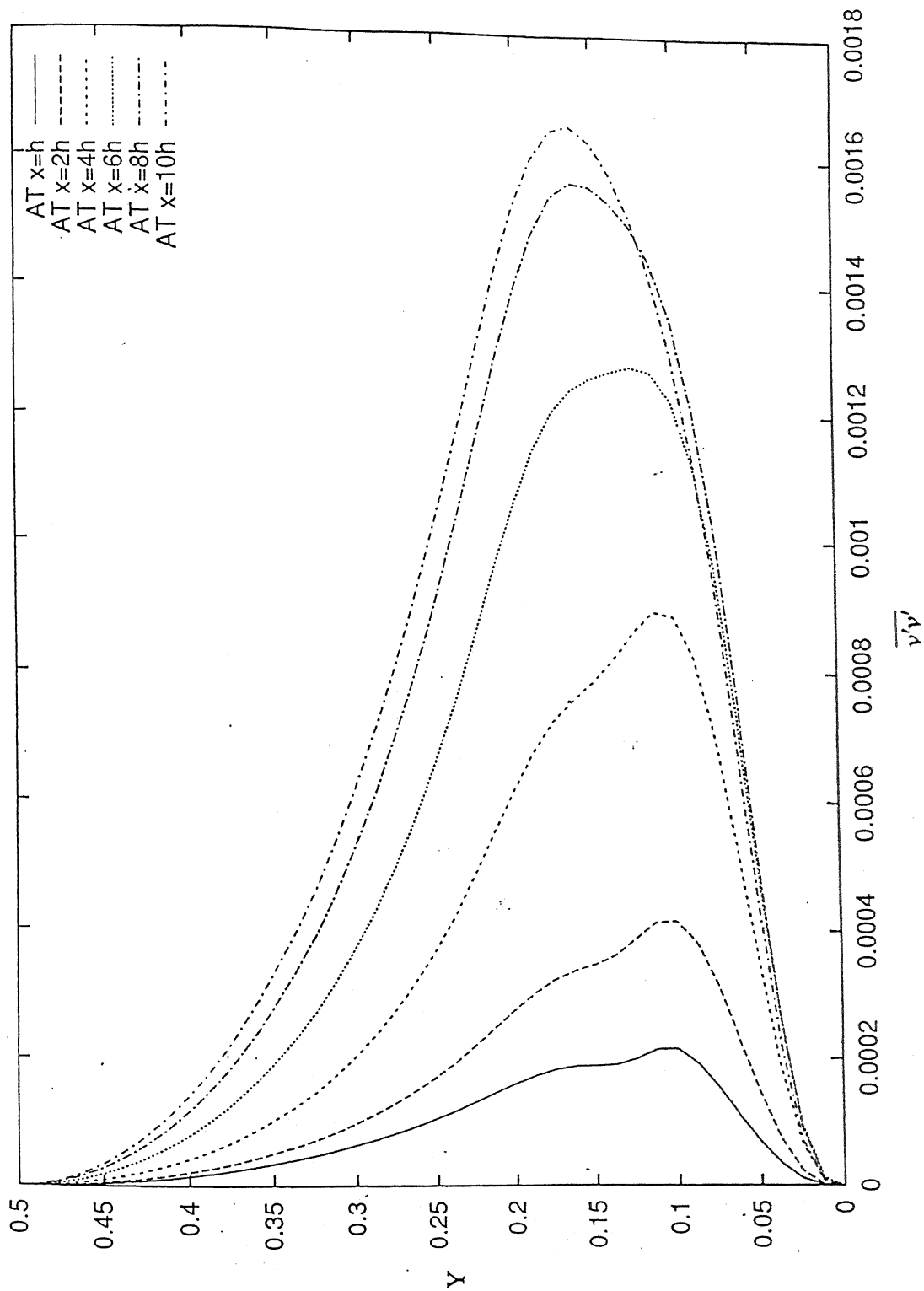


Figure 4.8 (a) Variation of time averaged transverse normal stress at different locations in the downstream

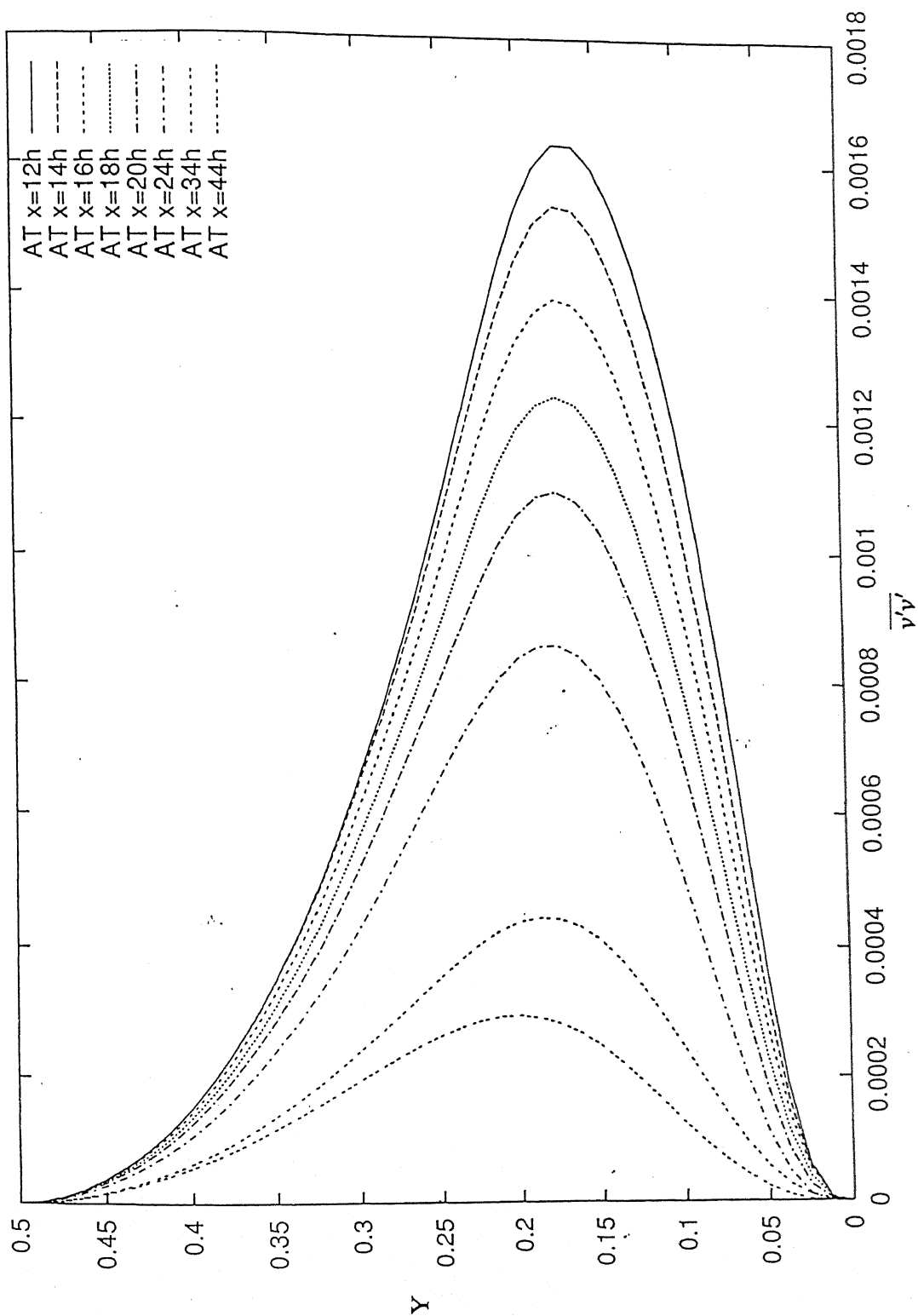


Figure 4.8 (b) Variation of time averaged transverse normal stress at different locations in the downstream

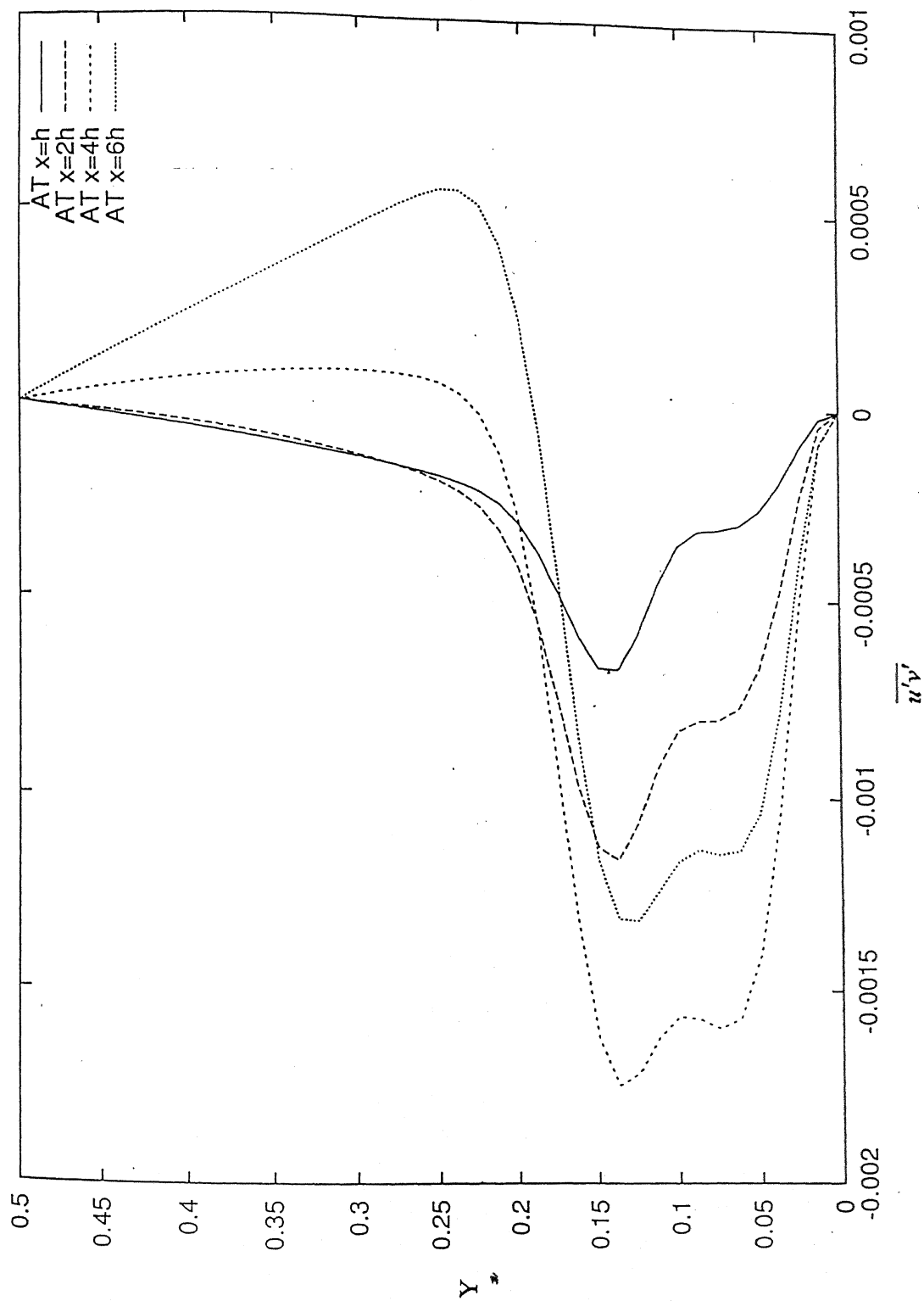


Figure 4.9 (a) Variation of time averaged shear stresses at different locations in the downstream

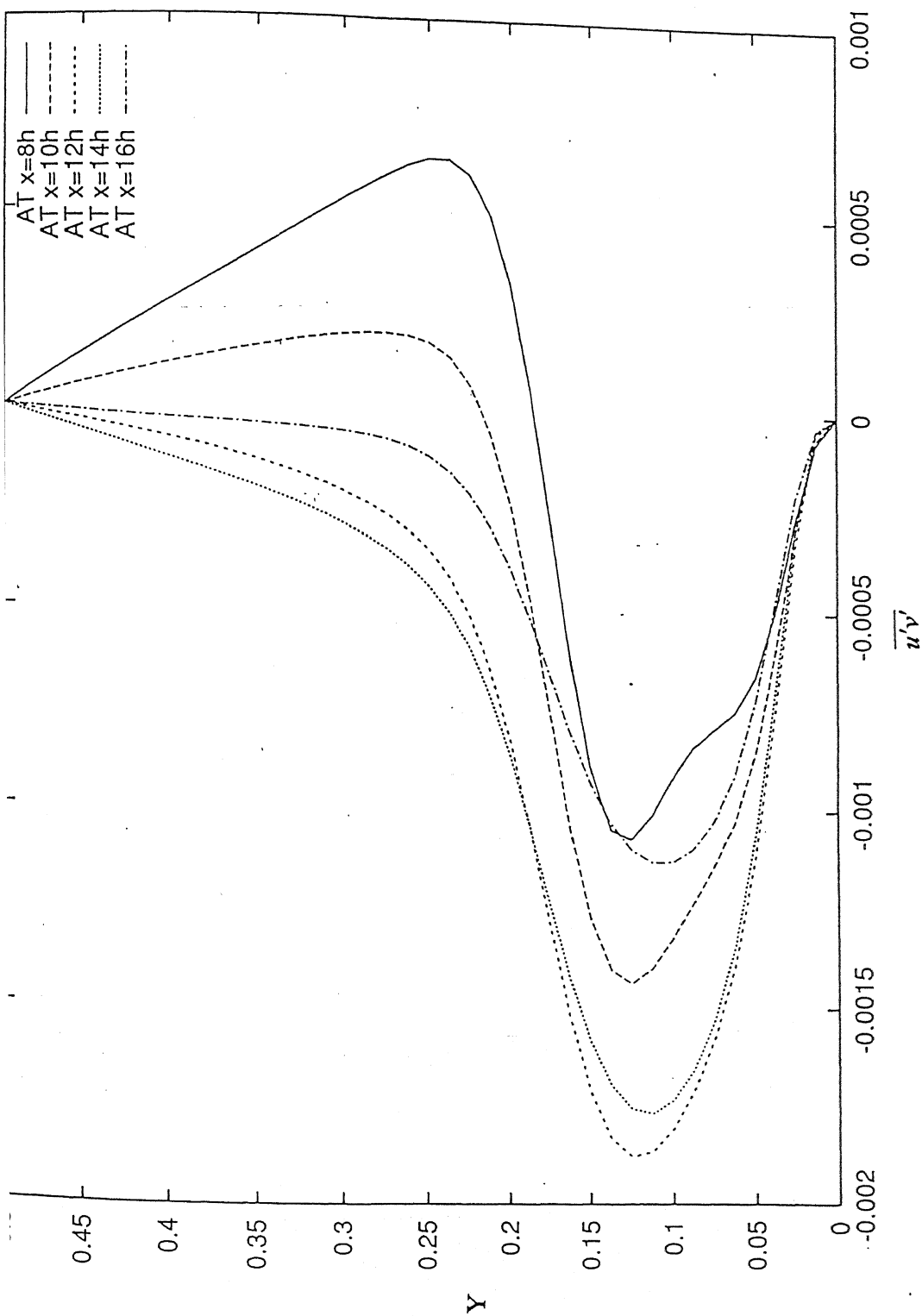


Figure 4.9 (b) Variation of time averaged shear stresses at different locations in the downstream

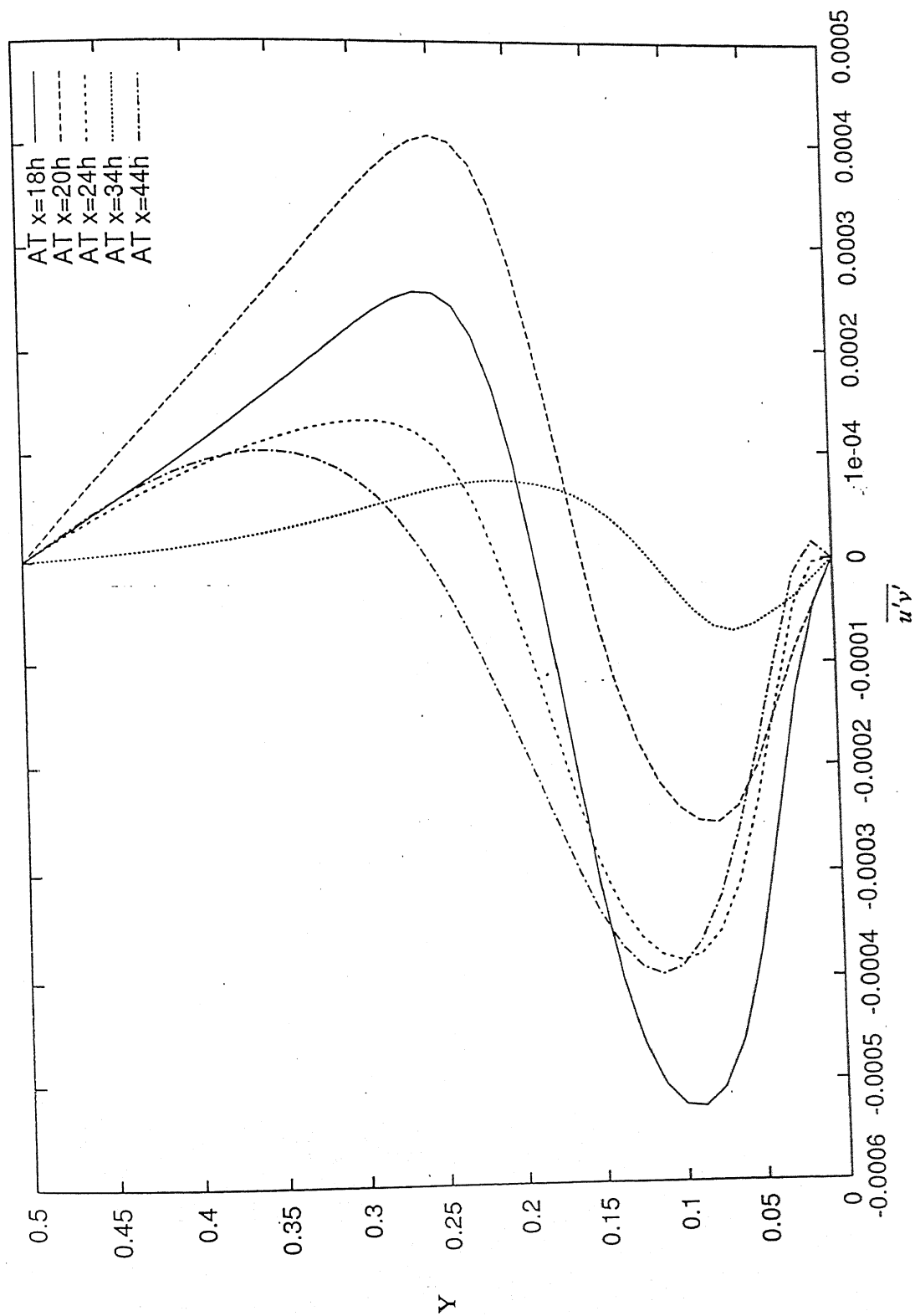


Figure 4.9 (c) Variation of time averaged shear stresses at different locations in the downstream

The average pressure distribution along the streamwise  $X$  – direction is shown in Fig.4.10. The pressure decreases and increases in the streamwise direction. The decrease in pressure distribution is due to the acceleration of flow which leads to corresponding decrease in pressure. The pressure again increases around the reattachment region due to beginning of the flow development. It should be noted that the surface pressure distribution presented by Vogel and Eaton (1985) for a backward facing step has similar variation with the exception that in the present case an undulation in the pressure distribution is observed after reattachment. This may be due to the fact that the average pressure presented here was obtained by averaging in both  $Y$  &  $Z$  directions and therefore contribution of fluctuation due to vortex shedding is seen in the average pressure distribution profile.

#### 4.5 Nusselt Number Distribution :

The spanwise average distribution of Nusselt number is presented in Fig.4.12. The Nusselt number is observed to be very high at the upstream corner of the rib. The Nusselt number decreases at the top surface of the rib and there is a sudden drop in its value in the near field region. There was a subsequent increase in the Nusselt number value in the far field region and the average value of the Nusselt number is higher than that of the plane channel case. This indicates the efficacy of the rib for heat transfer enhancement application. Vafai and Huang (1994) showed the Nusselt number variation on the top of intermittently emplaced porous cavity. The shape of their Nusselt number evolution is very much similar to that of the present case on the top of the rib surface.

#### 4.6 Power Spectra :

The power spectra of the  $v$  velocity is shown in Fig 4.12 for three different  $x/h$  location. The  $x/h$  location 2 and 10 corresponds to the pre-reattachment region. It should be noted that as expected, from the normal mode analysis, the amplitude of most amplified frequency decreases in the downstream direction. There is a presence of

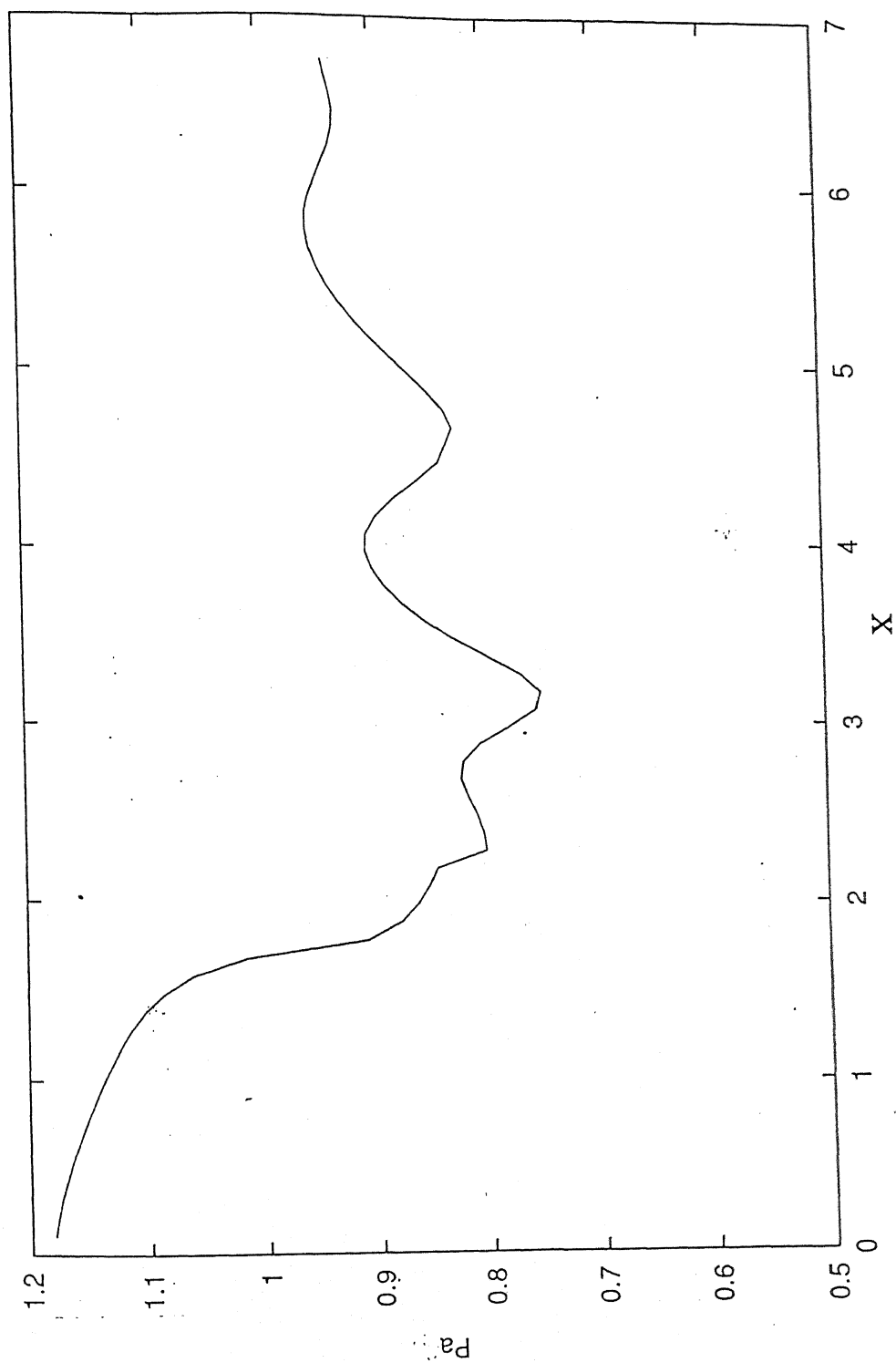


Figure 4.10 Average Non-dimensional Pressure Distribution along the length



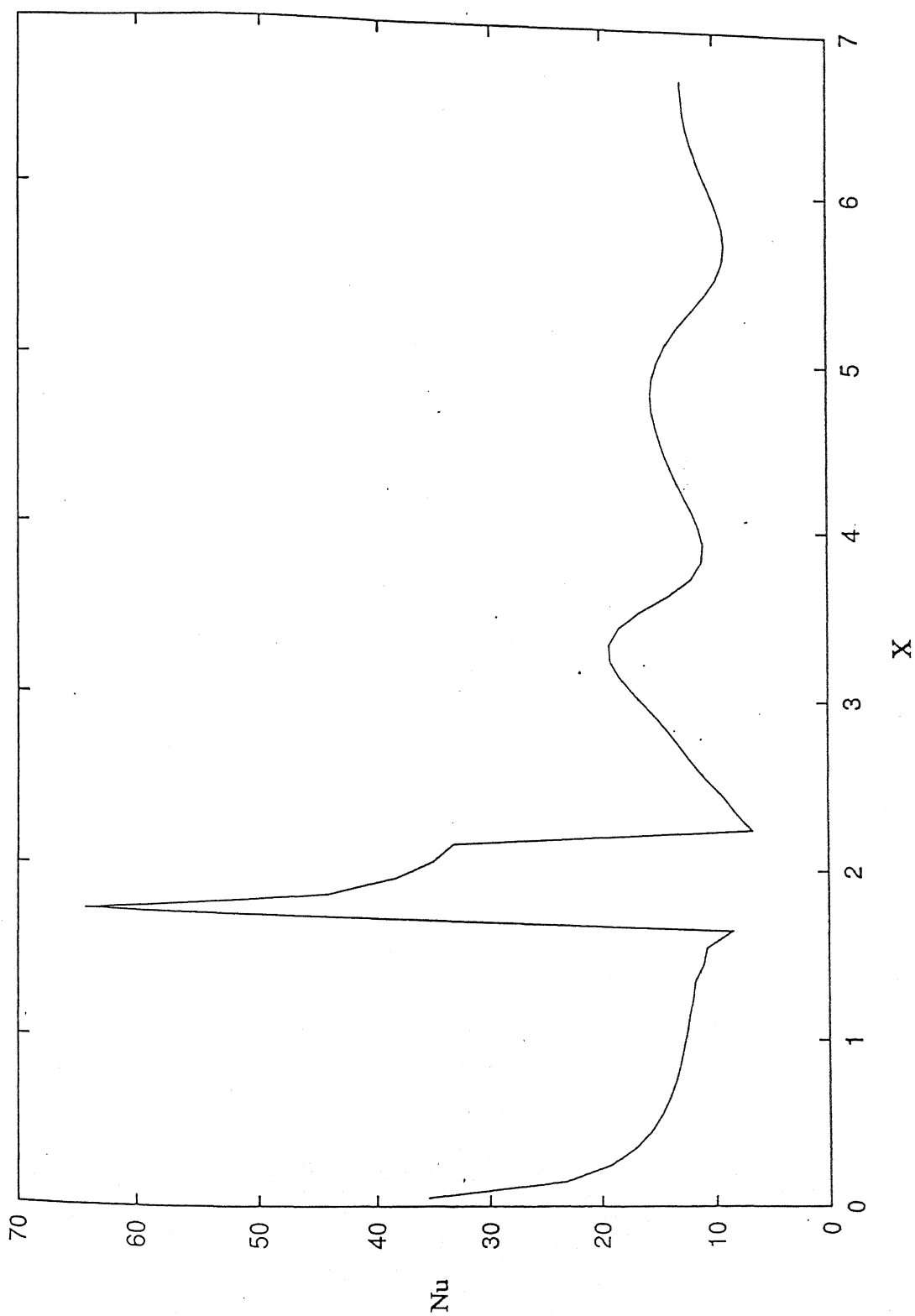


Figure 4.11 Spanwise average Nusselt number distribution along the length

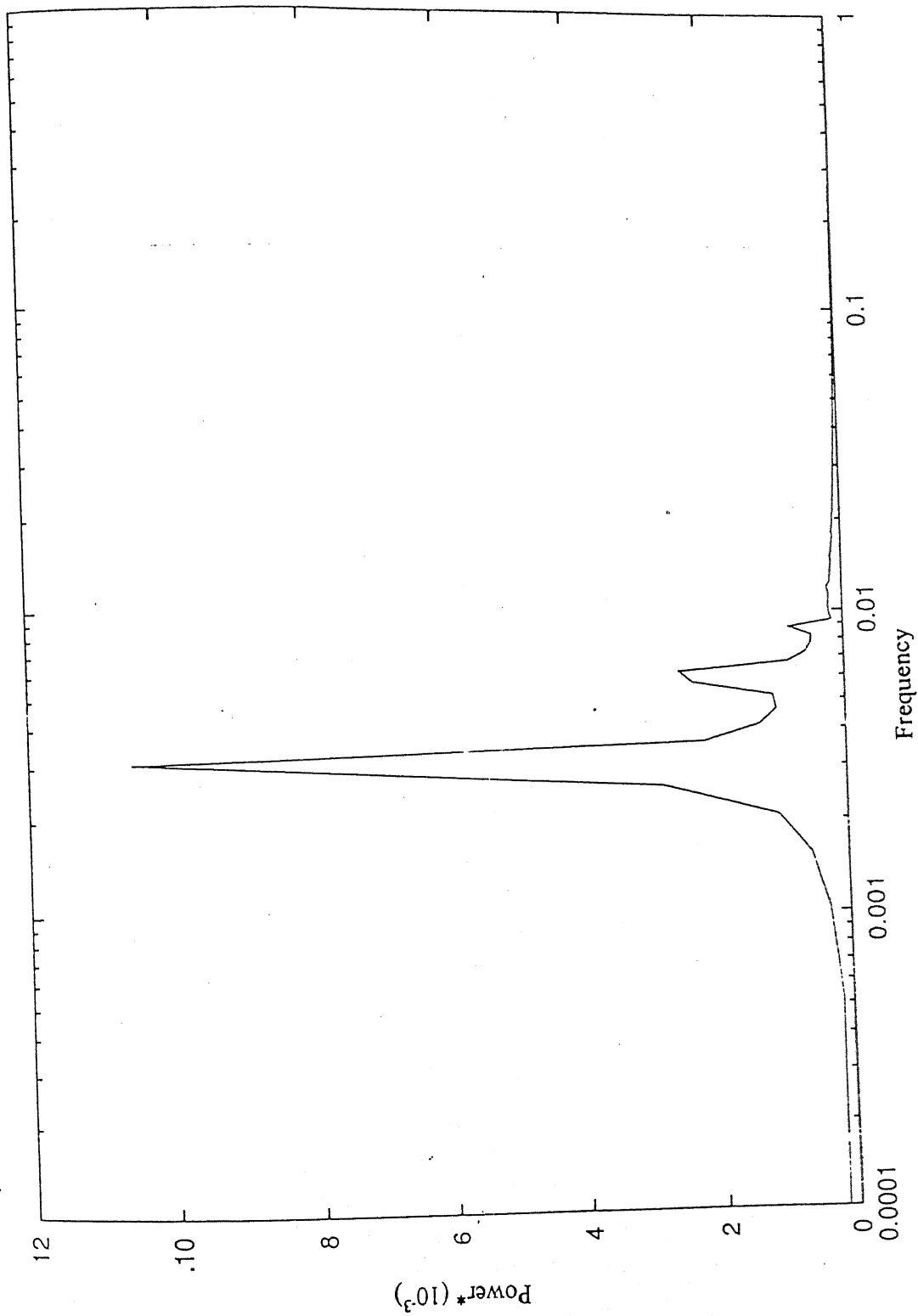


Figure 4.12 (a) Power Spectra at  $Re=2500$  at  $x=2h$ ,  $y=h/2$

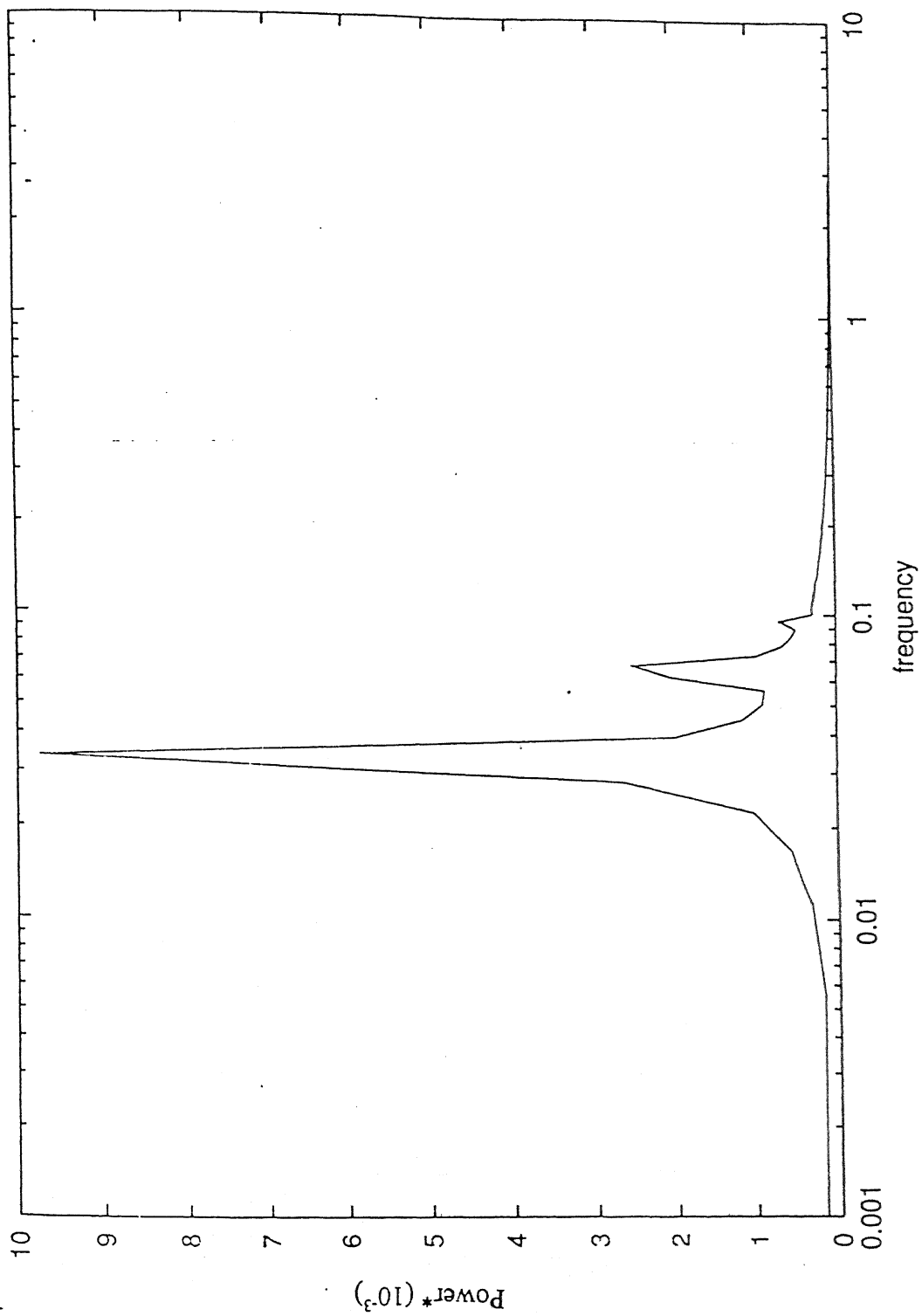


Figure 4.12 (b) Power Spectra at  $Re=2500$  at  $x=10h$ ,  $y=h/2$

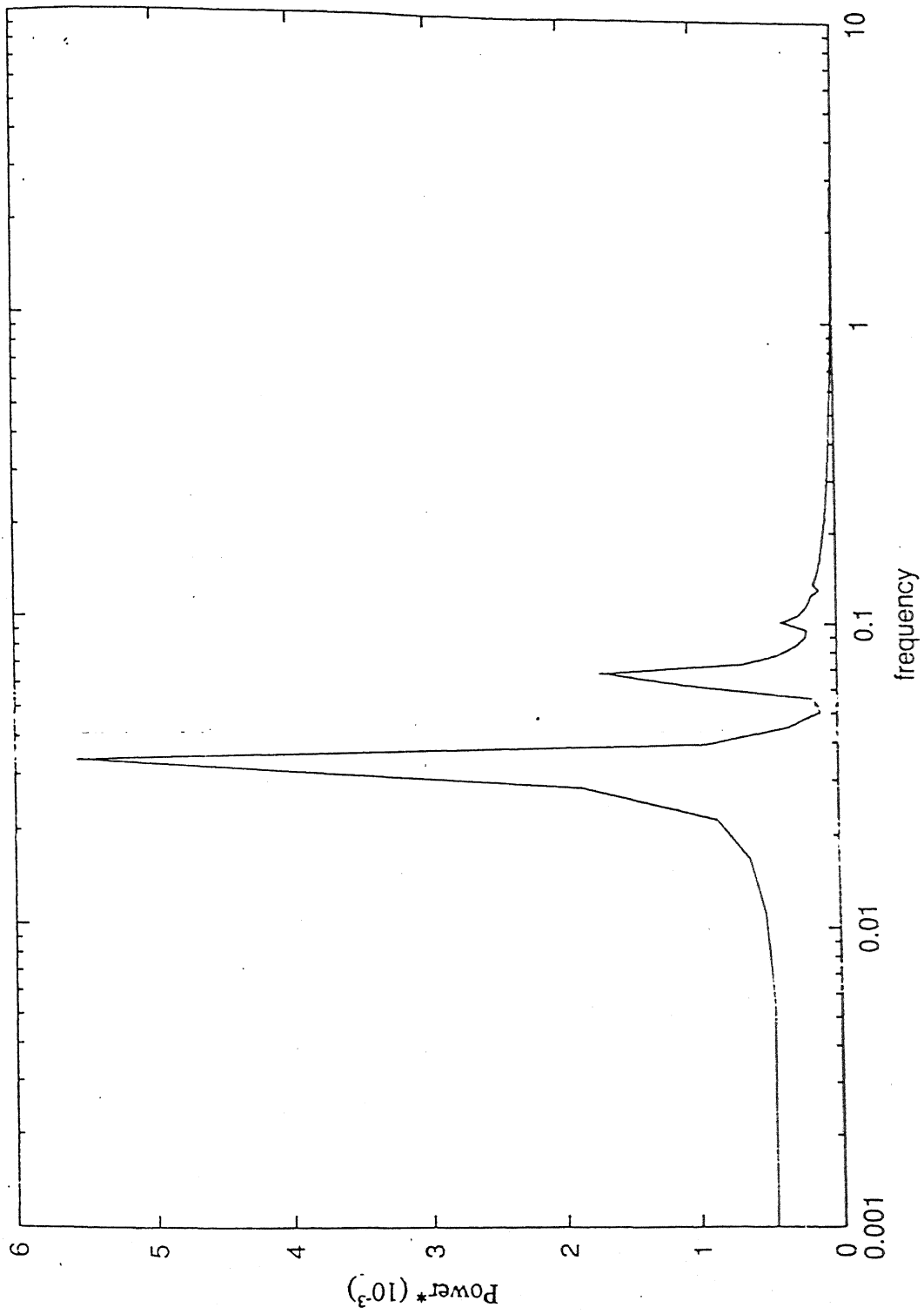


Figure 4.12 (c) Power Spectra at  $Re=2500$  at  $x=20h$ ,  $y=h/2$

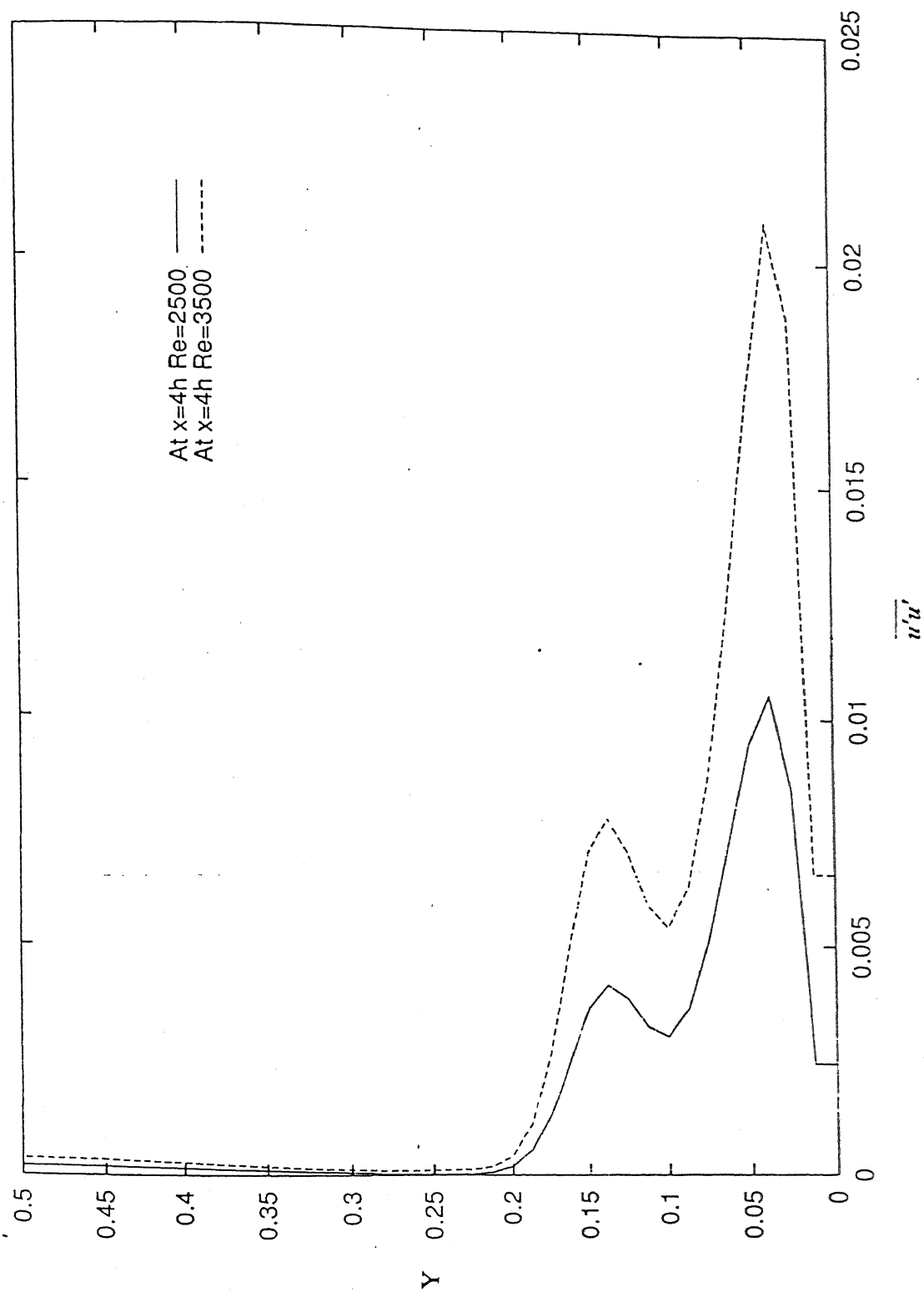


Figure 4.13(a) Variation of time averaged streamwise normal stresses at  $x/h=4$  at two different Reynolds number in the downstream

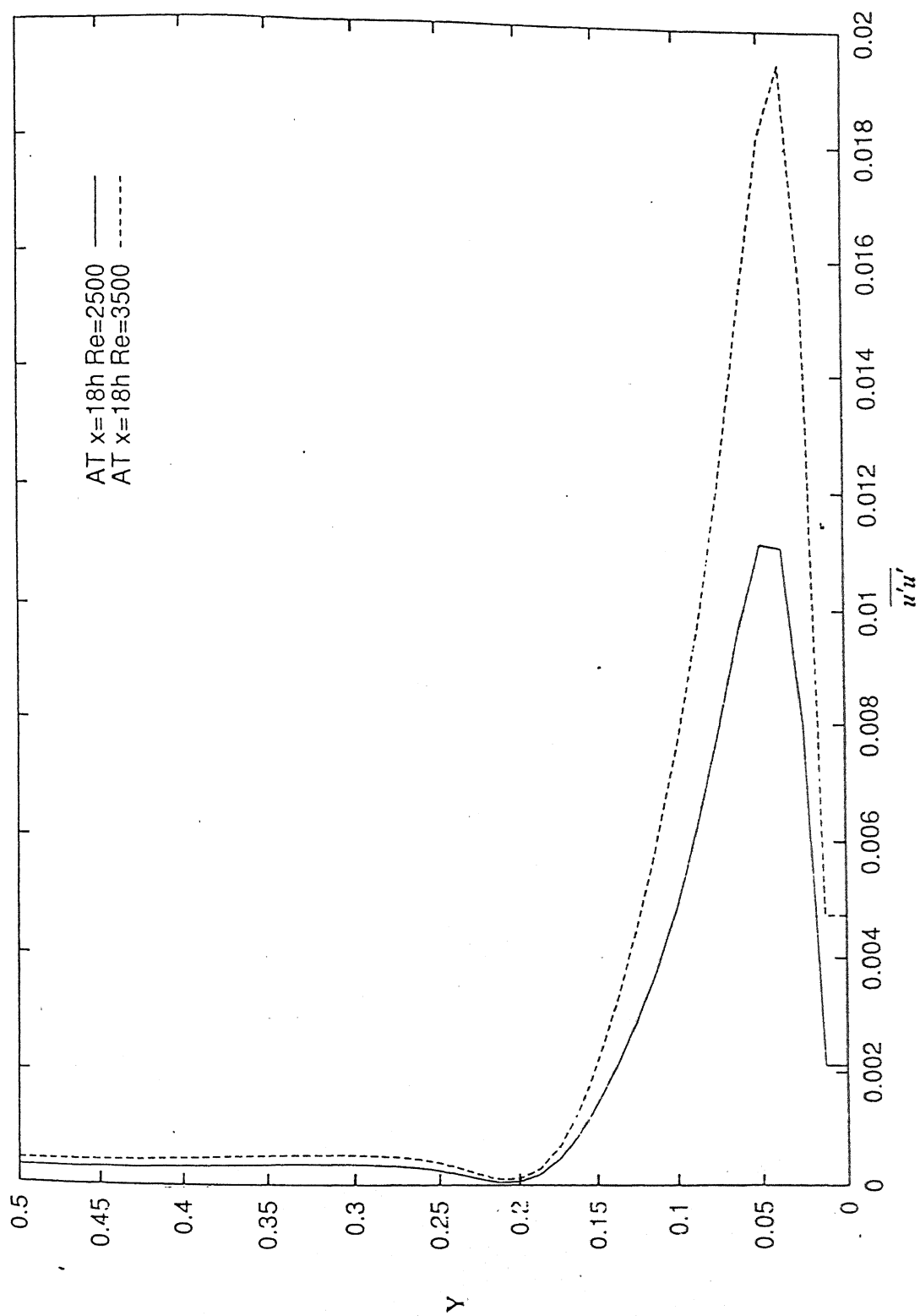


Figure 4.13(b) Variation of time averaged streamwise normal stresses at  $x/h=18$  at two different Reynolds number in the downstream

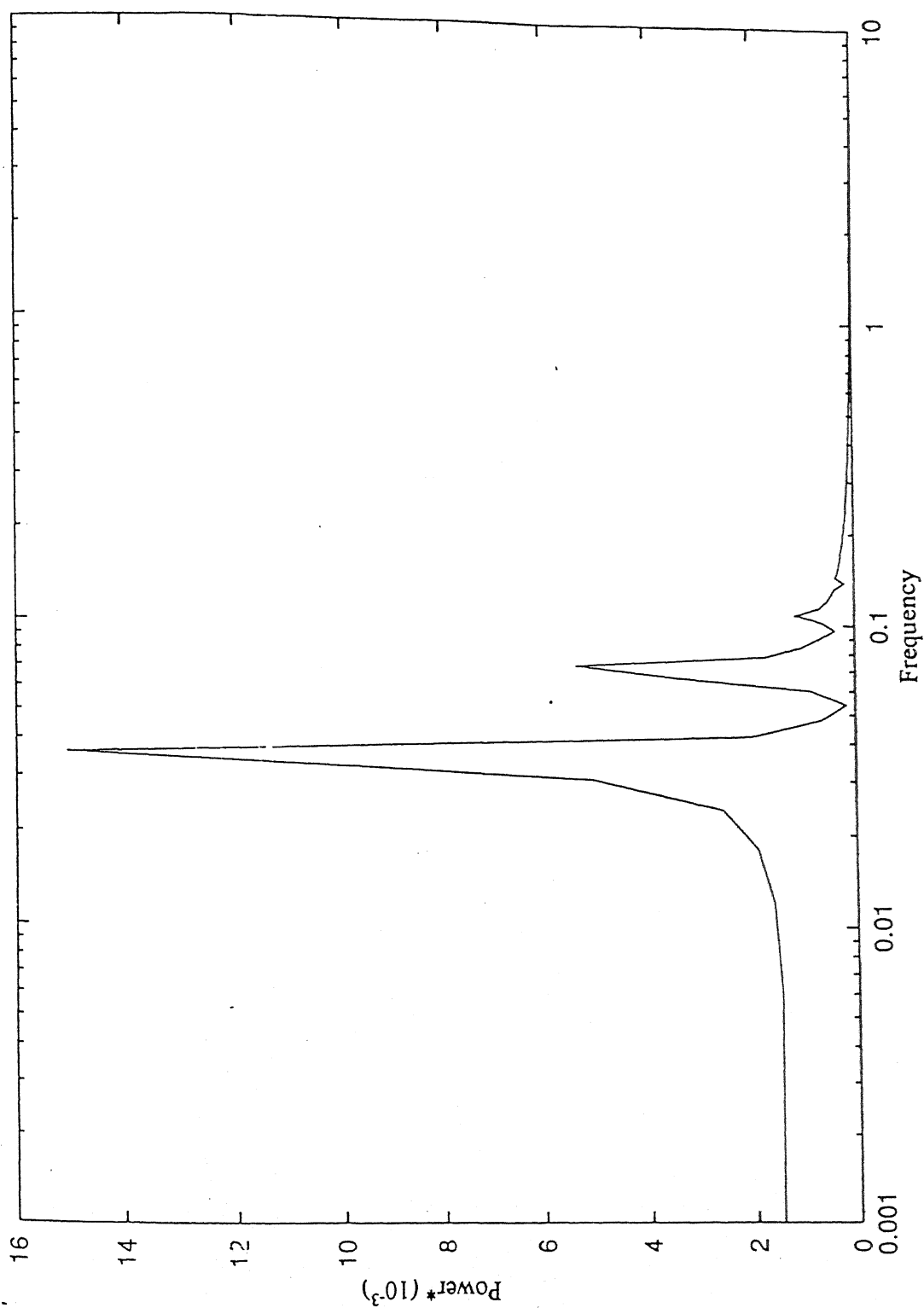


Figure 4.14 Power Spectra at  $Re=3500$  at  $x=2h$  and  $y=h/2$  at the spanwise midplane.

harmonic indicating the presence of nonlinearity in the evolution of the most amplified wave.

It may be noted that the non-dimensional frequency observed in this case is about 0.04 which is much less than the value of 0.12 observed for the rib in the free stream case. Similar drop in the non-dimensional frequency was observed by Arnal et. al. (1999) and Panigrahi (1997).

#### 4.7 Reynolds number effect

The effect of Reynolds number on the  $u_{rms}$  velocity is shown in Fig 4.13 for two different  $x/h$  locations. It is seen that as expected the maximum fluctuation is higher for higher Reynolds number case. To corroborate the variation, the power spectrum at  $x=2h$  is shown in Fig 4.14. Comparing Fig 4.14 with Fig 4.11 it is observed that the amplitude of the power spectrum is higher for the higher Reynolds number case.

This signifies that for higher Reynolds number the amplification of the most amplified frequency is higher and therefore there is a higher value of fluctuation for higher Re.

#### 4.8 Instantaneous Flow Fields

Figures 4.15 (a) and (b) show the velocity vector plot at the spanwise midplane after 6500 & 8500 time steps respectively. There is a big clockwise recirculating eddy just behind the obstacle and a small eddy downstream of the obstacle with the same sense of circulation as the previous one. These eddies signify the presence of vortices which are associated with high energy. The isovorticity plot at the spanwise midplane is shown in Fig 4.16. The primary spanwise Karman vortices  $\omega_z$  have been generated. Arnal et. al (1991) observed similar vortex shedding at  $Re=500$  for a rib placed on the fixed wall. At this point in the cycle, just after being shed from behind the rib the vortices move downstream. As they move downstream of the rib, their velocity gradually increases to the free stream velocity  $U_b$ . The vortices start pairing with those shed earlier and move downstream at the free stream velocity. As the vortices grow at their location



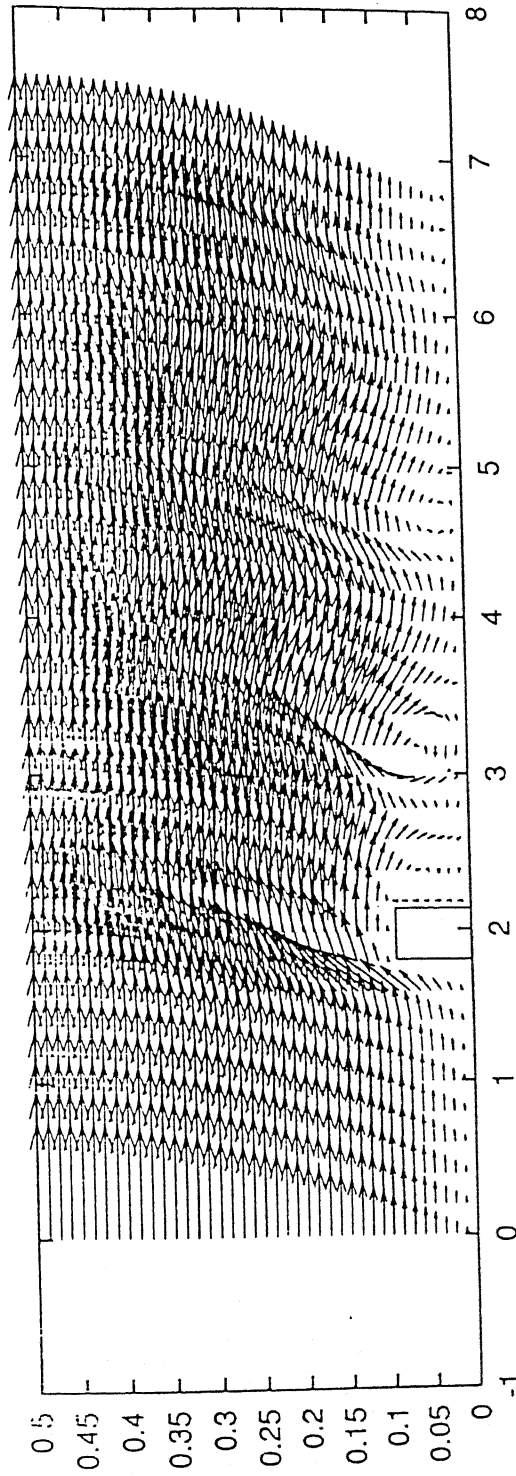


Figure 4.15 (a) Velocity vector plot at the spanwise midplane at  $t=6500$  time steps.

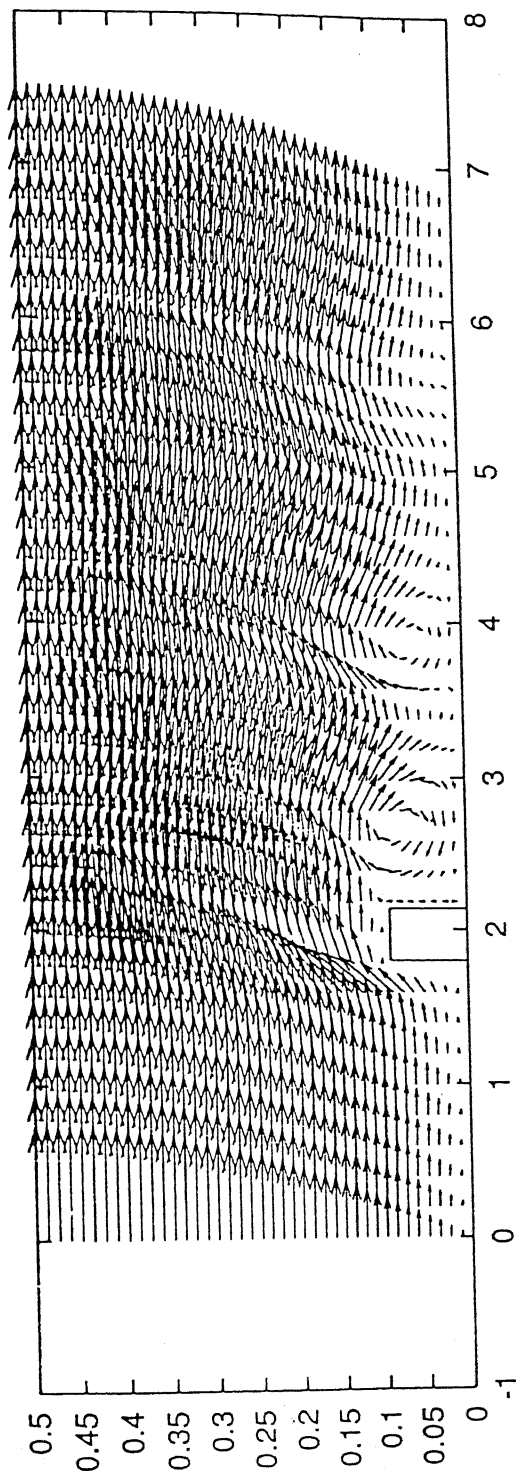


Figure 4.15 (b) Velocity vector plot at the spanwise midplane at  $t=8500$  time steps.

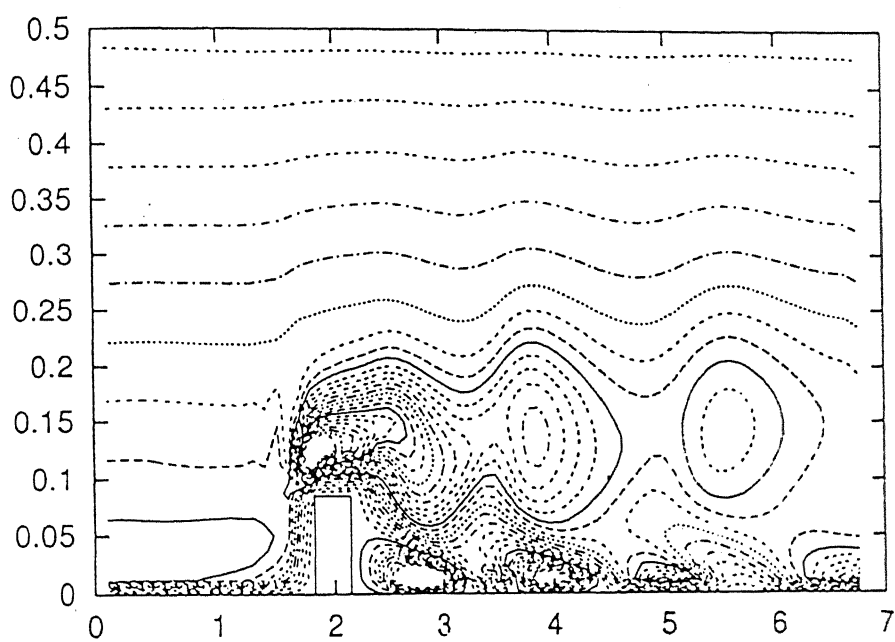


Figure 4.16(a) Instantaneous Isovorticity plot at Spanwise midplane at  $t=6500$  time steps.

$$\omega_{\min}, \omega_{\max}, \Delta\omega \equiv -5, 0.55, 15$$

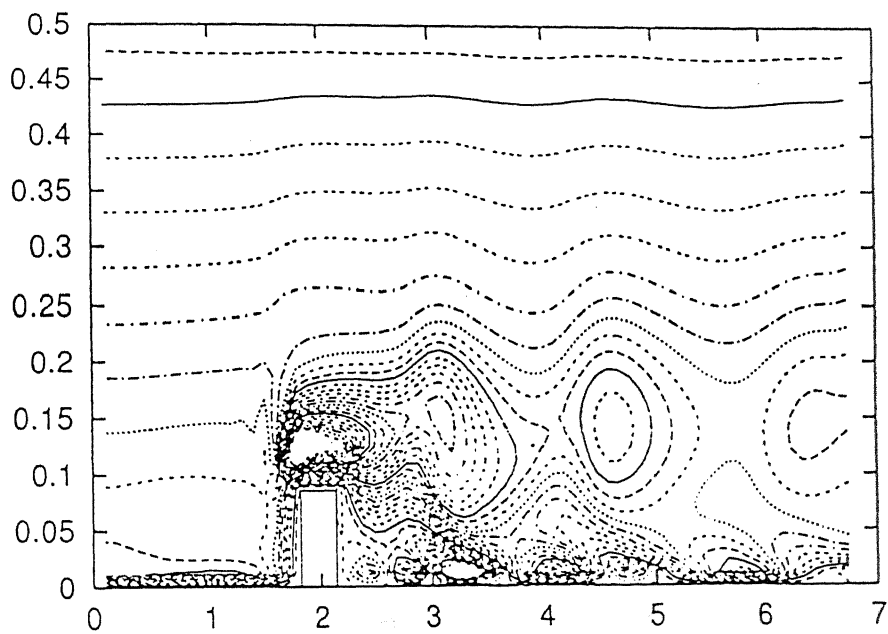


Figure 4.16(b) Instantaneous Isovorticity plot at Spanwise midplane at  $t=8500$  time steps.

$$\omega_{\min}, \omega_{\max}, \Delta\omega \equiv -5, 0.55, 15$$

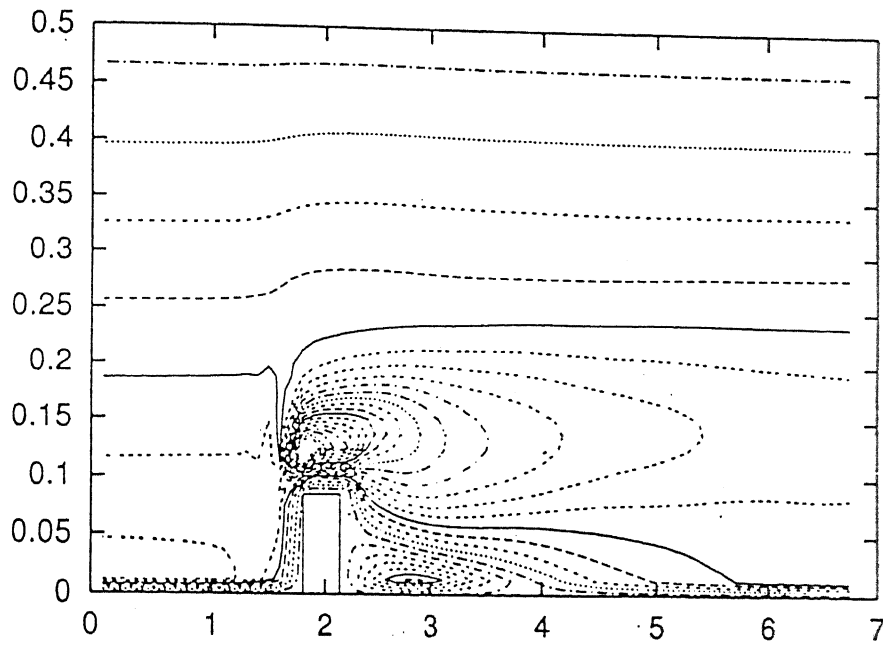


Figure 4.17 Time averaged vorticity plot at spanwise midplane.

$$\omega_{\min}, \omega_{\max}, \Delta\omega \equiv -5, 0.55, 15$$

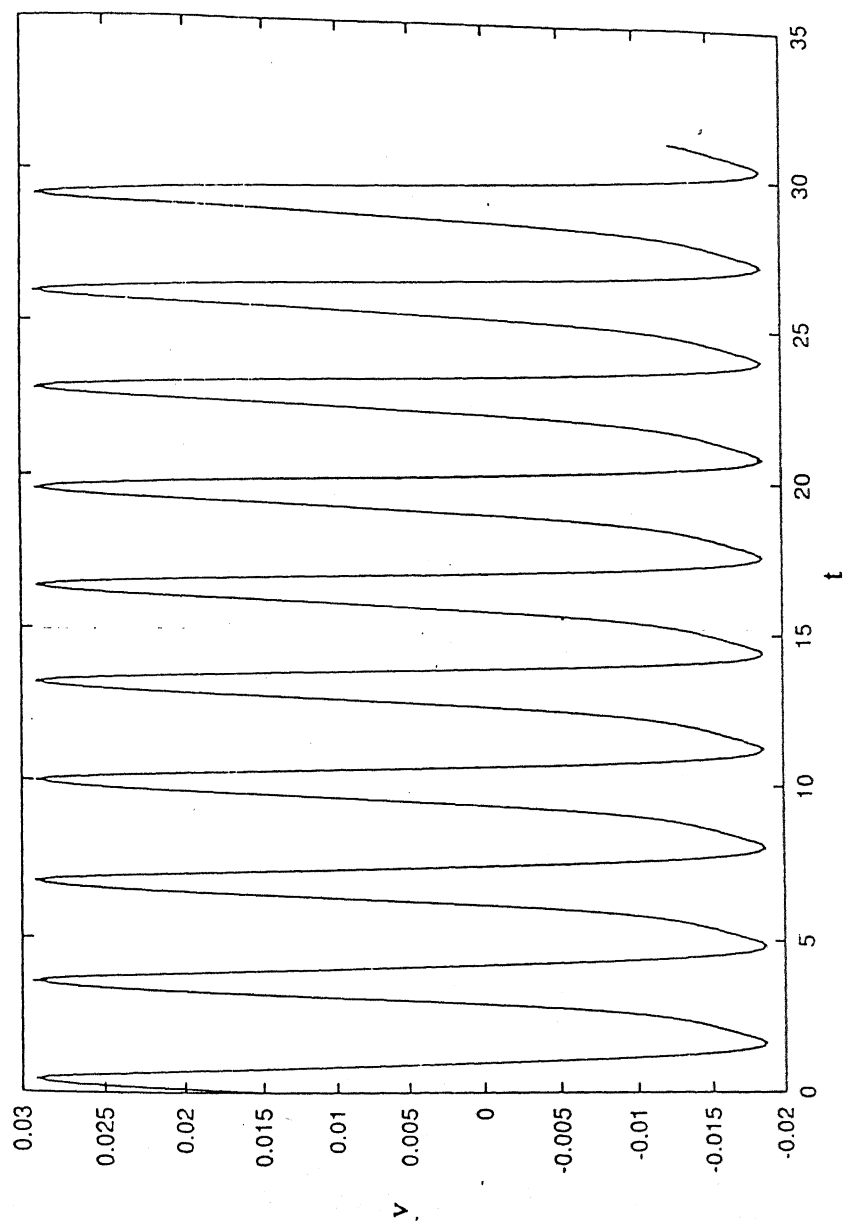


Figure 4.18 Velocity signal at Reynolds number 2500

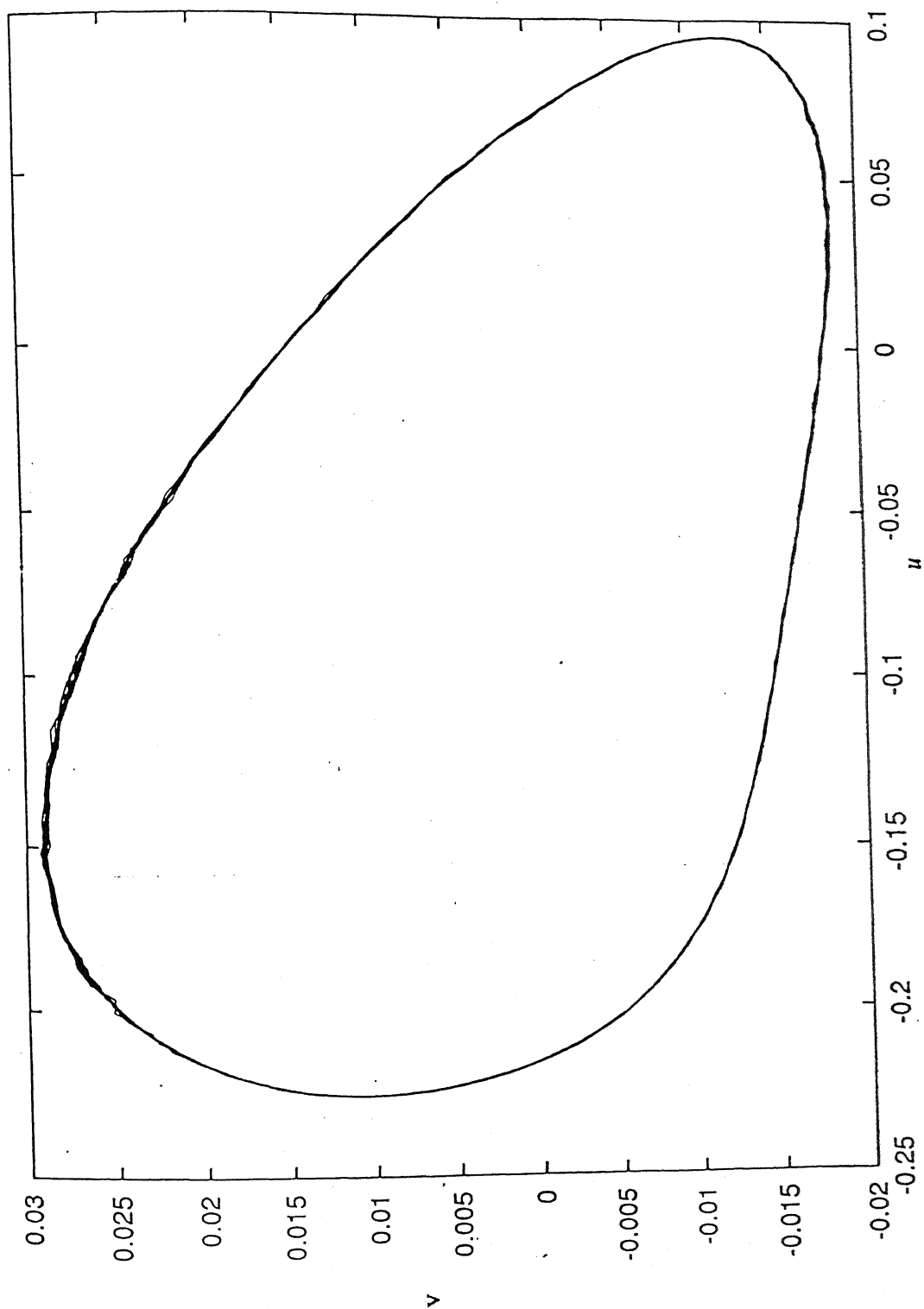


Figure 4.19 Phase plane plot at  $x=2h$ ,  $y=h/2$   $Re=2500$

behind the rib, the pressure on the downstream side of the rib gradually decreases as the fluid upstream is forced over the rib and the vortex pair. Both the positive and negative vortices were generated and the positive vortices are always found to be weaker than the dominant negative vortices generated by the shearing of the flow by the rib. The dominant negative vortices are found near the wall due to the effect of solid boundaries. Fig 4.17 shows the time averaged isovorticity plot at the spanwise midplane.

Figure 4.18 shows the time variation of the cross-stream velocity ( $v$ ) component. The velocities have converged asymptotically to a periodic state with fixed amplitude. The phase plane plot at  $Re=2500$  is shown in Fig 4.18. From this plot it is clear that the velocity is periodic and approaches a limit cycle. A similar limit cycle has been reported by Amon and Mikic (1990) in their analysis of flow through a communicating channel. This plot confirms that there is one dominant frequency in the flow field.



## CONCLUSIONS

Fluid flow and heat transfer results behind a surface mounted rib was investigated numerically in this work. Results showing the mean velocity, RMS velocity, power spectra, velocity contour, isovorticity contour, shear stresses, pressure distribution and Nusselt number were presented and compared with the existing numerical and experimental results wherever. Following conclusion are made from this investigation.

- (i). The reattachment shear layer behind the surface mounted rib is dominated by large-scale vortices. (ii) The Strouhal number describing the vortex shedding is not same as that of a rib in the free stream case. The Strouhal number behind a surface mounted rib is about 0.04 compared to the 0.12 value seen for a rib in the free stream. (iii) The average Nusselt number for the surface mounted rib is larger than that of a plane channel. (iv) There is an increase in the turbulence production with an increase in the Reynolds number. (v) The  $y$ -locations corresponding to the maximum  $u_{rms}$  velocity and  $v_{rms}$  velocity are not the same indicating that the effect of the bottom wall is more pronounced on the  $v$  velocity fluctuation. (vi) The reattachmment length of the reattaching shear layer is about 16 times the height of the rib. (vii) The general nature of velocity distributions and Reynolds Stresses are similar to the experimental results available from LDV measurements.

## SCOPE OF FUTURE WORK

- (i) Variable grid sizes need to be used in critical locations. (ii) The effect of rib width to rib height on the flow structures should be investigated. (iii) The effect of multiple ribs and the pitch between the ribs need to be studied. (iv) The effect of blockage ratio on the

fluid flow should be studied. (v) The effect of rotation similar to actual gas turbine blade should be studied. (vi) The three dimensionality of the flow structure should be presented by performing detailed analysis. (vii) Techniques like Pattern recognition method, Phase averaging, VITA and Enhanced VITA should be used to characterize the large-scale structures. (vii) The true length scale for the calculation of Strouhal number should be investigated.

## References

1. Harlow and Welch, 1985, ' Numerical Calculation of Time-Dependent Viscous Incompressible Flow of Fluid with Free Surface' *The Physics of Fluids*, Vol 8, pp. 2182-2189.
2. Patankar S.V., Liu C.H., Sparrow E.M., 1977, ' Fully Developed Flow and Heat Transfer in Ducts having Streamwise Periodic Variations of Cross-Sectional Area ' *ASME Journal of Heat Transfer*, Vol 99, pp. 180-186.
3. Bergeles G. and Athanassidis N., 1983 ' The Flow Past a Surface-Mounted Obstacle ' *Journal of Fluids Engineering* , Vol 105, pp. 461-463.
4. Vogel J.C. and Eator J.K., 1985 ' Combined Heat Transfer and Fluid Dynamic Measurement Downstream of a Backward Facing Step ' *ASME Journal of Heat Transfer*, Vol 107, pp. 922-929.
5. Tropea C.D. and Gackstatter R., 1985 ' The Flow over Two-Dimensional Surface Mounted Obstacles at Low Reynolds Numbers ' *Journal of Fluids Engineering* , Vol 107, pp. 489-484.
6. Ghaddar N.K., Korczak K.Z., Mikic B.B. and Patrea A.T., 1986 ' Numerical Investigations of Incompressible Flow in Grooved Channels ' *Journal of Fluid Mechanics* , Vol 163, pp. 99-127.
7. David M.D., Seegmiller H.L., 1987 ' Time Dependent Behaviour of a Reattaching Shear Layers ' *AIAA* , Vol 25, pp. 914-919.
8. Kelkar K.M., Patankar S.V., 1987 ' Numerical Prediction of Flow and Heat Transfer in a Parallel Plate Channel with Staggered Fins ', *Journal of Heat Transfer* , Vol 109, pp. 25-30.
9. Liou T.M. and Kao C.F., 1988, ' Symmetric and Assymetric Turbulent Flows in a Rectangular Duct with a Pair of Ribs, ' *Journal of Fluids Engineering* , Vol 110 pp. 373-379.

10. Antonion J. and Bergeles G., 1988 ' Development of Reattached Flow Behind Surface Mounted Two-Dimensional Prism, ' *Journal of Fluids Engineering* , Vol 110, pp. 127-133.
11. Han J.C., 1988 ' Heat Transfer and Friction Characteristics in Rectangular Channel with Rib Turbulators ', *Journal of Heat Transfer* , Vol 110, pp. 321-328.
12. Arnal M.P. and Goering D.J., 1991 ' Vortex Shedding from a Bluff Body Adjacent to a Plane Sliding Wall ', *Journal of Fluids Engineering* , Vol 113, pp. 384-397.
13. Durao D.F.G., Gouveia P.S.T. and Pereiro J.C.F, 1991 ' Velocity Characteristics of Flow around a Square Cross Section Cylinder Placed near a Channel Wall ', *Experiments in Fluids* , Vol 11, pp. 341-350.
14. Acharya S., Myrum T.A. and Inamdar S., 1991 ' Subharmonic Excitation of the Shear Layer Between Two Ribs; Vortex Interaction and Pressure Field ', *AIAA Journal* , Vol 29, pp. 1390-1399.
15. Amon C.H., Mikic B.B., 1990, ' Numerical Prediction of Convective Heat Transfer in Self Sustained Oscillatory Flows ', *Journal of Thermophysics* , Vol 4, pp. 239-246.
16. Garimella S.V. and Eibeck P.A, 1991 ' Fluid Dynamics Characteristics of Flow over an Array of Large Roughness Elements ', *Journal of Electronics Packaging* , Vol 113, pp. 367-373.
17. Majumdar D. and Amon C.H., 1992 ' Heat and Momentum Transport in Self Sustained Oscillatory Viscous Flows ' *Journal of Heat Transfer* , Vol 114, pp. 866-873.
18. Myrum T.A., Acharya S., Inamdar S. and Mehrotra A., 1992 ' Vortex Generator Induced Heat Transfer Augmentation Past a Rib in a Heated Duct Air Flows ', *Journal of Heat Transfer* , Vol 114, pp. 280-284.
19. Biswas G. and Chattopadhyay H., 1992 ' Heat Transfer in a Channel with Built-in Wing type Vortex Generatrions ', *Int. Journal of Heat and Mass Transfer*, Vol 35, pp. 803-814.

20. Chang B.H. and Mills A.F., 1993 ' Turbulent Flows in a Channel with Transverse rib Heat Transfer Augmentation ' *Int. Journal of Heat and Mass Transfer*, Vol 36, pp. 1459-1469.
21. Acharya S., Dutta S., Myrum T.A. and Baker K.s, 1994 ' Turbulent Flow Past a Surface Mounted Two-Dimensional Rib ', *Journal of Fluids Engineering* , Vol 116, pp. 238-245.
22. Vafai K. and Huang P.C., 1994 ' Analysis of Heat Transfer Regulation and Modification Employing Intermittency Emplaced Porous Cavities ', *Journal of Heat Transfer* , Vol 116, pp. 604-613.
23. Prakash C. and Zerkle R., 1995 ' Prediction of Turbulent Flow and Heat Transfer in Ribbled Rectangular Duct with and without Rotation ', *Journal of Turbomachinery* , Vol 117, pp. 255-264.
24. Dejong N.C., Zhang L.W., Jacob A.M., Balachandar S. and Taffi D.K, 1998 ' A Complementary Experimental and Numerical Study of the Flow and Heat Transfer in Offset Strip-Fin Heat Exchangers ', *Journal of Heat Transfer* , Vol 120, pp. 690-698.
25. Jem-Siang Hwang, 1998 ' Heat Transfer-Friction Characteristic Comparison in Rectangular Ducts with Slit and Solid Ribs Mounted on One Wall ' *Journal of Heat Transfer* , Vol 120, pp. 709-716
26. Chiang T.P. and Tony W.H., 1999 ' A Numerical revisit of Backward Facing Step Flow Problem ', *Physics of Fluids* , Vol 11, pp. 862-874.